Rebecca Eells, David P. Hoogerheide, Paul A. Kienzle,
Mathias Lösche, Charles F. Majkrzak, Frank Heinrich

3 Structural investigations of membrane-associated proteins by neutron reflectometry

Abstract: Neutron reflectometry (NR) is a powerful technique for probing the structure of lipid bilayer membranes and membrane-associated proteins. Measurements of the specular neutron reflectivity as a function of momentum transfer can be performed in aqueous environments, and inversion of the resulting reflectivity data yields structural profiles along the membrane normal with a spatial resolution approaching a fraction of a nanometer. With the inherent ability of the neutron to penetrate macroscopic distances through surrounding material, neutron reflectivity measurements provide unique structural information on biomimetic, fully hydrated model membranes and associated proteins under physiological conditions. A particular strength of NR is in the characterization of structurally and conformationally flexible peripheral membrane proteins. The unique ability of neutron scattering to differentiate protium from selectively substituted deuterium enables the resolution of individual constituents of membrane-bound protein–protein complexes. Integrative modeling strategies that supplement the low-resolution reflectometry data with complementary experimental and computational information yield high-resolution three-dimensional models of membrane-bound protein structures.

3.1 Introduction

With both researchers in the life sciences and interested students in mind, this chapter provides an overview of theoretical and practical aspects of neutron reflectometry (NR) from biomimetic lipid membranes that enables the structural characterization of membrane-bound proteins. We focus on peripheral membrane proteins,

Rebecca Eells, Department of Physics, Carnegie Mellon University, Pittsburgh, USA
David P. Hoogerheide, Paul A. Kienzle, Center for Neutron Research, National Institute of Standards and Technology, Gaithersburg, USA
Mathias Lösche, Department of Physics, Carnegie Mellon University, Pittsburgh, USA; Center for Neutron Research, National Institute of Standards and Technology, Gaithersburg, USA; Department of Biomedical Engineering, Carnegie Mellon University, Pittsburgh, USA
Charles F. Majkrzak, Center for Neutron Research, National Institute of Standards and Technology, Gaithersburg, USA
Frank Heinrich, Department of Physics, Carnegie Mellon University, Pittsburgh, USA; Center for Neutron Research, National Institute of Standards and Technology, Gaithersburg, USA

https://doi.org/10.1515/9783110544657-003

which are challenging systems to investigate by conventional structural biology methods due to the thermodynamic nature of their interaction with the lipid membrane and their structural and conformational flexibility. At the same time, they are particularly well amenable to the characterization with neutrons. While the theory of NR and many of the discussed protocols are directly applicable to integral membrane proteins, we do not cover the difficult problem of integral membrane protein reconstitution into lipid membranes.

3.1.1 Cellular membranes and proteins

In their most fundamental role, membranes constitute the boundaries of a cell that separate the cytoplasm from the extracellular environment and partition the cell internally into regions of different functionality, i.e., the organelles. However, this function is far from being a passive one, as cellular membranes play active and essential roles in processes such as cell signaling, selective transport between compartments they separate, information transduction and processing, and cellular morphogenesis. To perform these functions, cellular membranes consist of complex mixtures of phospholipids and proteins [1], which can be membrane-integral or membrane-peripheral [2]. Integral membrane proteins often span the entire bilayer, that is, they are transmembrane proteins [3, 4]. Peripheral proteins do not predominantly interact with the hydrophobic core of the lipid bilayer, but rather associate with the lipid headgroups and with other membrane proteins via a multitude of hydrophobic, electrostatic, and bio-specific contacts [5]. Peripheral membrane association of these proteins is often reversible, such that there is an equilibrium between membrane-associated and cytosolic states that may depend on the status of the cell. Peripheral membrane proteins often assume multiple conformations depending on their environment, and interactions between the protein and the membrane, even if merely transient, can induce structural rearrangements or function-related conformational changes [6]. Furthermore, stochastic motions of disordered protein regions can play important functional roles.

Considering their importance for cellular function, it is not surprising that membrane protein malfunction is implicated in a wide variety of diseases, including cystic fibrosis [7], type-2 diabetes [8], heart disease [9], neurological disorders [10], and cancer [11]. The penetration of toxins and pathogens into the cell also involve protein–membrane interactions [12, 13]. Acting as an efficient, selective barrier between the cell and its environment, membranes manage mostly to keep such incursions at bay. However, in an evolutionary tug o' war, many pathogens develop specificity for binding to proteins on their host target cell membranes to gain entry, thereby circumventing or hijacking the cell's defense mechanisms. As a result, about half of current drug targets are membrane proteins [2], and certain classes of membrane proteins, such as G-protein coupled receptors (GPCRs), are among the most

actively investigated targets of current drug development [14]. The ability to identify new drug targets and develop new therapeutics has been limited by a lack of high resolution, three-dimensional structures. While membrane proteins comprise ≈30% of mammalian proteomes, their structures determined so far provide only ≈1% of the entries in the Protein Data Bank (PDB) [15].

3.1.2 Challenges in structural biology of membrane proteins

The three major techniques to obtain high-resolution (atomic-level) protein structures are cryo-electron microscopy (cryo-EM), nuclear magnetic resonance (NMR), and X-ray diffraction (XRD). The majority of membrane protein structures has been determined with XRD from protein crystals grown in detergent [15]. In such crystals, detergent molecules associate with protein surfaces that are natively embedded in a lipid bilayer. However, membrane protein structures are, at least in part, determined by the proteins' interactions with these environments and may depend on the biophysical properties of the native membrane [16]. Therefore, it is often difficult to assess how well detergent contacts approximate the native lipid environment.

As an alternative to the use of detergents in XRD, membrane proteins can be embedded in lipid bicelles [17, 18] or in lipidic cubic phases (LCP) [19]. In particular, recent developments in LCP technologies ranging from precrystallization assays to data collection, as well as the commercial availability of tools to utilize these technologies, have the potential to drastically increase the number of structures obtained from detergent-free samples [20, 21]. For proteins with large extra-membrane domains, a liquid analog of LCP, known as the sponge phase, has been used [22]. Two major technical challenges for the LCP crystallization approach remain in harvesting the crystals and data collection due to the small crystal size [20].

NMR has proven invaluable for the determination of high-resolution structures and dynamics of soluble proteins and solubilized membrane proteins [23, 24]. Both solution and solid-state NMR can be applied to study integral and peripheral membrane proteins. For solution NMR, micelles, bicelles, or nanodiscs can provide a lipid membrane environment. However, large-weight complexes of membrane proteins with micelles or bicelles often tumble too slowly to permit the fast rotational diffusion needed to obtain well-resolved spectra [24]. Solid-state NMR (ssNMR), in principle, does not have the same molecular weight constraint as solution NMR, and well-resolved spectra are achieved through magic angle spinning or by oriented sample spectroscopy [16, 25]. With ssNMR, proteins can be characterized within a bilayer environment mimicking the native membrane such as liposomes [25] or oriented membranes [26]. However, most membrane protein structures solved with this technique so far have been limited to molecular weights less than 10 kDa due to the complexity of the ssNMR spectra [24, 27]. Sample heterogeneity and dynamics can also impose limits on ssNMR measurements since they lead to broadened resonances

and spectral overlap. Sensitivity enhancement techniques such as ^{1}H detection, dynamic nuclear polarization, and nonuniform sampling algorithms are recent developments that will extend the applicability of ssNMR toward larger proteins [25].

Cryo-EM is the third major structural method for membrane proteins. While cryo-EM was limited to the investigation of large complexes in the past, recent improvements in instrumentation, such as the direct electron detection camera, and image processing resulted in increased resolution, lower size limits, and better classification of heterogeneous samples [15, 28]. Thus, cryo-EM allows for the characterization of membrane proteins in a lipid bilayer environment at resolutions that, in some cases, are comparable to resolutions achieved by XRD.

3.1.3 Neutron reflectometry

NR for biological systems is a well-established technique [29–35], and all major neutron scattering facilities worldwide have biological NR capability [36–38]. In comparison with the high-resolution techniques in structural biology discussed above, NR provides distinct advantages for characterizing in-plane disordered, fluid lipid membranes and the association of membrane proteins in fully buffer-immersed biomimetic environments. While NR is intrinsically a low-resolution technique, when complemented with high-resolution methods and MD simulation, atomistic detail of biomimetic protein–membrane complexes is obtained. NR has been successfully applied to study intrinsically disordered proteins and peptides [39–44], and peripheral membrane proteins that may only associate with the membrane transiently (see Figure 3.1) [45–57]. The ability of neutron scattering to use selective deuteration to highlight parts of the structure allows for the characterization of individual constituents of membrane-bound protein–protein complexes [58]. Since NR is nondestructive, the sample can be manipulated *in situ* during a series of measurements. By changing environmental conditions, biological processes can be simulated, for example, through the introduction of cofactors or by applying external cues [52], and the evolution of the system can be monitored.

NR yields one-dimensional structural profiles along the normal direction of the interface from which the beam is reflected. In investigations of membranes deposited at such an interface, the compositional profile represents in-plane averages parallel to the bilayer at each position along the normal direction, thus yielding a temporal and spatial ensemble over all molecular configurations (see Section 3.2). NR requires planar substrates of low surface roughness that carry the interfacial structure of interest, as well as samples that are homogeneous and stable over typically hour-long measurements. The development of biomimetic, in-plane fluid sparsely tethered lipid membranes (stBLMs) for NR [59–63] has addressed this requirement (see Section 3.3). Conducting the NR experiment requires specialized sample environment that allows for in situ sample manipulation and maximizes the signal-to-noise ratio of the

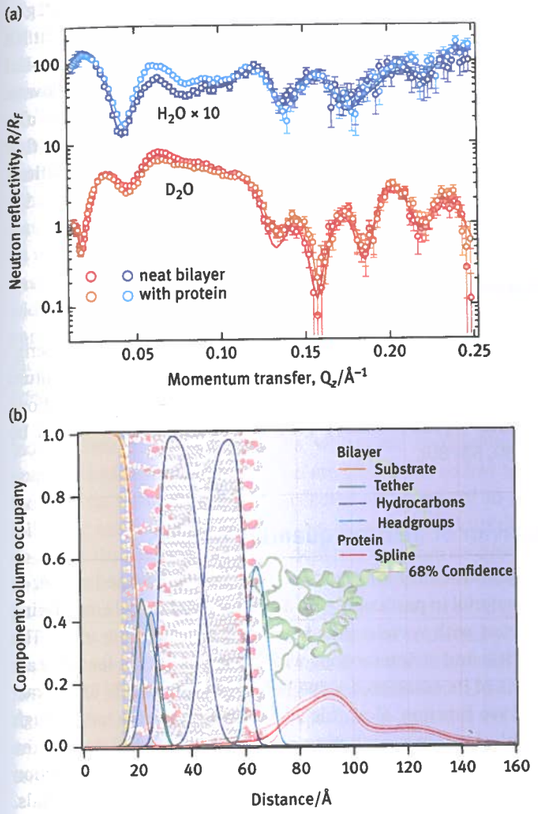

Figure 3.1: Neutron reflection measurements of the peripheral membrane protein HIV-I Gag matrix on a sparsely tethered bilayer lipid membrane. (a) NR reflectivities of the membrane, immersed in two isotopically distinct (H_2O and D_2O-based) buffers before and after incubation with protein. All data were measured on one membrane sample, such that all four measurements could be used to refine one general model structure. (b) Component volume occupancy profiles along the bilayer normal of the membrane–protein complex from a composition-space model. The profile of the protein was determined using a free-form spline (red traces) and localizes the compact core and flexible tail of the protein with respect to the lipid bilayer. In a more refined model, the orientation of the protein was subsequently determined by rigid body modeling using an ensemble of NMR structures (PDB: 2H3F). The background image is a visual representation of the protein on the membrane surface that derives from this refined analysis. (Figure adapted from Eells et al. [46].)

measurement (see Section 3.5). The implementation of molecular modeling strategies [64, 65] in the recent decade has transformed the technique [33]. With a current NR setup, structural features with a thickness of 10 Å can be resolved with a spatial resolution of a fraction of an nm, and volume occupancies of components as low as 5–10% at any position along the surface normal can be reliably determined. A fully atomistic interpretation can be achieved with integrated modeling strategies that utilize complementary experimental data and molecular dynamics (MD) simulations [49, 56, 66, 67] (see Section 3.5).

3.2 Fundamentals of neutron reflectometry

We begin by reviewing the remarkably accurate physical and mathematical description of specular reflection which, in practice, reduces to a one-dimensional quantum mechanical scattering process. This theory is described without detailed derivations of the relevant mathematical equations since comprehensive expositions can be readily found elsewhere [30, 68–80].

3.2.1 Wave-like behavior of neutron quantum objects

It so happens that to obtain structural information about soft condensed matter in general – and biological material in particular – on a subnanometer scale, scattering methods employing neutrons with wavelengths between 1 and 10 Å are ideal. The neutron is a quantum particle and its interactions with matter on such a length scale must be described in terms of its associated wave behavior, specifically as characterized by the neutron's wave function. How this wave function is affected through interaction with a material object in a scattering process can be predicted by the Schrödinger equation of motion in a probabilistic manner. The neutron interaction with matter is predominantly via the nuclear potential in nonmagnetic materials. Experimentally obtained scattering patterns must be analyzed mathematically to deduce the corresponding structure of the scattering object. In essence, this is common to all wave diffraction methods, including X-ray and neutron crystallography. In contrast, methods that image objects in real space, such as optical and electron microscopy, use particles with wavelengths that are far shorter than the objects' spatial dimensions so that wave diffraction effects are negligible. The length scale probed by neutron reflectivity is about an order of magnitude larger than the neutron wavelength, that is, of the order of a nanometer rather than an Angstrom. This means that the potential representing the interaction between a neutron and the scattering structure, such as a lipid membrane with embedded proteins, is effectively continuous, varying smoothly as a function of distance, except at well-defined boundaries, for example, between material and vacuum or aqueous reservoir.

The wave function associated with a freely propagating neutron quantum particle, as it might be found in a beam on a scattering instrument, is localized and occupies a finite volume of space (at least for the practical purposes of interest here). This localized wave function is referred to as a wave packet and typically has dimensions of the order of a fraction to tens of microns, depending on how the particular state was prepared after emission from a source, for example, by monochromating crystals and angle-defining pairs of apertures [81]. This neutron wave packet can be described mathematically by a coherent superposition of basis states, often taken to be a normal distribution of plane waves each having a given value of wave vector $\boldsymbol{k}$, whose magnitude $k = 2\pi/\lambda$ depends on the neutron wavelength λ of the state. The width of the distribution of the packet's basis wave vectors along a given direction in space is inversely proportional to the width of the probability amplitude distribution of where the neutron quantum particle is located along that same direction. This is a fundamental expression of the well-known uncertainty principle of quantum mechanics [82]. Each packet representing an individual neutron in the beam has an associated mean wave vector $\bar{\boldsymbol{k}}$. In practice, the neutrons composing a beam can be taken to be an ensemble of independent individual members which are completely noninteracting with one another. Incident beam intensities are oftentimes so low that a single given neutron incident on a sample object is reflected and captured in a detector before the next following neutron in the beam is even incident. The Schrödinger wave equation which describes the scattering of an incident neutron from a material object is explicitly time-dependent, specifically in terms of what happens to the neutron's associated wave packet before and after. However, since we are interested in the structure, and not the dynamics of biological interfaces, only elastic scattering processes are relevant. Here, the total energy of the neutron is conserved and it is possible to solve a simpler, time-independent wave equation using single plane wave (steady-state) representations of the neutron. Nonetheless, it is important to consider the finite spatial extent of the neutron wave packet when interpreting experimentally measured reflectivity data in terms of the steady-state solutions, as will be discussed in the following section.

3.2.2 Specular neutron reflectivity and the scattering length density profile

The neutron reflectivity R is defined as the number of neutrons reflected from a nominally flat interface, divided by the number of neutrons incident at a glancing angle (typically several degrees) from that interface (Figure 3.2). Specular reflection occurs when the glancing angles of incidence (I) and reflection (F) are equal to one another so that the momentum and wave vector transfer, $\boldsymbol{Q} = \boldsymbol{k}_F - \boldsymbol{k}_I$, are along the surface normal. If the interface is perfectly smooth and the materials at the interface are characterized by a homogeneous in-plane density distribution, only specular scattering can occur. If, on the other hand, in-plane inhomogeneity does exist, then

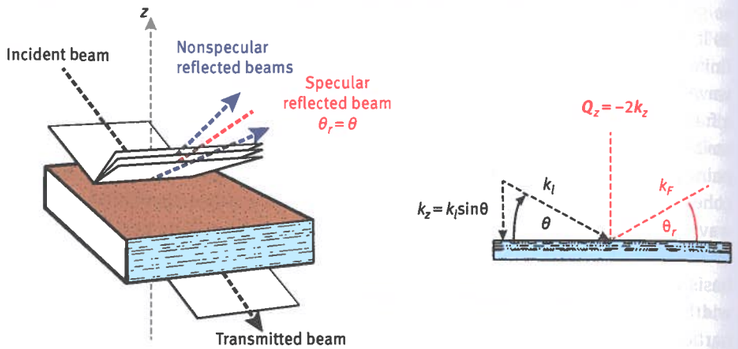

Figure 3.2: Scattering configuration for reflection at glancing angles of incidence. Specular reflection occurs when the angles of incidence and reflection are equal to one another so that the momentum and wave vector transfers are along the nominal surface normal. The neutron reflectivity $R(\theta)$ is defined as the ratio of the number of incident neutrons over that of the specularly reflected neutrons as a function of incident angle θ.

the specular signal gives the in-plane average over an area equal to the projected transverse coherent extent of the neutron wave packet wave fronts [81], and some incident neutrons will contribute to nonspecular scattering. If this nonspecular component remains small, it can be neglected to a good approximation; however, if it is large, a more elaborate analysis is required. For the systems of interest here, we limit our discussion to specular reflection and corresponding in-plane-averaged compositional depth profiles along the interface normal.

The complex reflection amplitude r is the specularly reflected neutron wave function related to the neutron scattering length density (nSLD) profile along the nominal normal direction to the planar film structure. The nSLD for a given material is the sum of the numbers, per unit volume, of nuclei of each specific constituent element multiplied by its corresponding scattering power, as characterized by a scalar coherent scattering length, which has been determined and tabulated for most isotopes [83].

However, only the reflected intensity, that is, the complex square of the reflection amplitude $R = |r|^2$ expressed as a function of wave vector transfer, $R(Q_z)$, with $Q_z = 4\pi \sin\theta/\lambda$, can be directly measured. R corresponds to the probability of finding a neutron quantum particle scattered into a particular angle. In turn, the reflectivity $R(\theta)$ for a model nSLD profile can be obtained via solution of the one-dimensional Schrödinger wave equation. This allows for fitting a parameterized nSLD model to a measured reflectivity as a function of glancing angle, $R(\theta)$ [30]. Any solution for the nSLD profile thereby obtained is not guaranteed to be unique because of the lack of phase information in R. To remove such ambiguity, either additional, independent information about the sample, or multiple measurements with composite systems

that include known structural parts such as a reference layers of known scattering properties are required (see Section 3.2.3).

An arbitrary nSLD profile can be subdivided into n layers, each of a specified thickness d over which the nSLD value is approximated to be constant. The smaller the d becomes, the larger is the range of wave vector transfer Q_z over which the reflectivity must be measured to resolve differences in nSLD on that spatial length scale. This follows from a straightforward, semiquantitative consideration of the Fourier relationship between real and scattering (reciprocal) space, which exists in the Born approximation solution for the reflectivity [84]. The same approximate relationship between r and the nSLD profile also affords a means to approximate the uncertainty in the values of nSLD obtained for a given statistical accuracy in the reflectivity data measured [84]. Figure 3.3 illustrates schematically the relationship between the specular reflectivity and nSLD for a measurement performed on α-hemolysin [85] embedded in a lipid bilayer membrane [66].

In practice, the smallest resolvable length scale in NR is roughly determined by the maximum momentum transfer, Q_z^{max}, of the measurement, or the value of Q_z at which the specular reflection becomes comparable to the measurement background, whichever is smaller. The spatial resolution of a measurement with such a Q_z^{max} is approximately π/Q_z^{max}, or about 13 Å for the data shown in Figure 3.3a ($Q_z^{max} = 0.25\,\text{Å}^{-1}$). This should be compared to the intrinsic resolution limit determined by the root mean square roughness of the substrate (typically ≈ 3 Å for a silicon substrate, but potentially much larger for additional deposited layers). Rough surfaces also reduce the Q_z at which the reflected intensity drops below the background intensity [86]. Thus, smooth substrates and minimal background are central to obtaining high-quality density profiles.

Knowing the sizes of each distinct area of different SLD in the plane of the film is important. As discussed in Section 3.2.1, it is necessary to know over what in-plane area the neutron packet wave front is capable of coherently averaging. This is determined by the transverse extent of the wave front – at a sufficiently uniform phase – that is projected onto the sample surface. In one limit, at which each individual neutron averages over all different types of in-plane areas, a single coherent specular reflectivity signal will be measured. In the opposite limit, if each neutron can only view one of a number of distinct regions of a given SLD at a time, then the measured reflectivity will correspond to an area-weighted incoherent sum of the reflectivities for each type of in-plane region. In either case, an appropriate analysis of the data can be performed with sufficient knowledge of the in-plane SLD distribution. Figure 3.4 illustrates in-plane averaging pictorially. It is preferable to prepare a sample with the greatest in-plane homogeneity possible on a length scale comparable to the projected transverse extent of a neutron packet wave front: a contiguous film has advantages over one with islands.

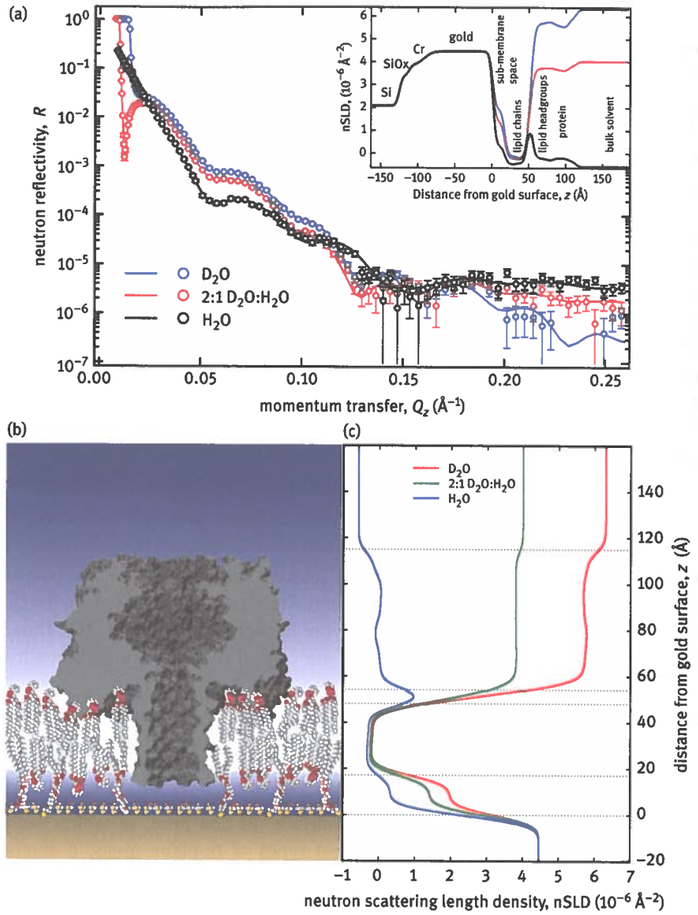

Figure 3.3: Relationship between the specular reflectivity and nSLD profile for a measurement performed on α-hemolysin in a tethered lipid bilayer membrane (see Section 3.3.1) prepared on a solid (silicon / silicon oxide / chromium / gold) substrate. (a) The measured neutron specular reflectivity for various mixtures of H_2O and D_2O in the aqueous reservoir adjacent to the lipid bilayer. Inset: nSLD profiles corresponding to the three measurements with isotopically distinct buffers, across the entire sample obtained by a simultaneous fit of all measured reflectivity curves. (b) Rendering of the bilayer and protein structure based on the nSLD profiles. (c) Magnification of the nSLD profiles across the lipid bilayer region, scaled to the depiction in (b). (Figure adapted from McGillivray et al. [66].)

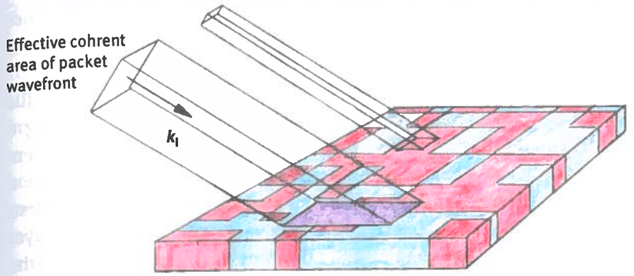

Figure 3.4: The effective transverse coherence area perpendicular to the propagation direction of the neutron wave packet is projected onto the film surface defining an area over which in-plane variations in nSLD are averaged in the specular process (note that the glancing angle of incidence enhances the projection along one in-plane direction). The length scale of the nSLD variations must be small enough for averaging to occur within the projected area. The purple shaded area represents the coherent average of separate areas of "red" and "blue" nSLD. If the length scale of the nSLD variations are not small enough, then the net measured reflected intensity $|r|^2$ is an area-weighted sum of reflectivities, each corresponding to an in-plane averaged SLD within a particular respective area, as depicted schematically for the case of two distinct areas of different SLD (red and blue areas). For a typical reflectometer, the neutron is prepared such that the transverse coherent extent of the wave front is on the order of a micrometer.

3.2.3 Uniqueness and phase information

The inherent loss of explicit phase information is a problem common to all diffraction measurements, but often additional, independent knowledge about the structure and composition of the system is sufficient to eliminate ambiguities. In other cases, a unique solution can be obtained through isomorphic substitution of constituent atoms, for example, by varying the SLD of a surrounding fluid reservoir or solid supporting substrate, or by implementing external references such as neighboring, distinct layers in a multilayered film structure [84, 87–92]. This entails collecting multiple reflectivity data sets, each corresponding to a composite system consisting of a common layered part of interest, the structure or composition of which is unknown, plus a reference part that is completely known. The real and imaginary parts of the reflection amplitude r for the unknown part of interest alone can be mathematically determined, uniquely and independently at each given value of Q_z. Once the amplitude r is obtained, a direct inversion to obtain the corresponding unique nSLD profile can be performed in a model-independent way through the solution of an integral or differential equation, to the extent that sufficiently accurate data up to an appropriate value of Q_z can be measured. Alternatively, the reflectivity data sets from the composite system can be simultaneously fit [92]. Both approaches

yield the same unique nSLD profile within numerical and statistical accuracy since both are sensitive to the essential phase information contained within the composite system reflectivity data.

Figure 3.5 shows an example of direct inversion whereby the nSLD profile was extracted from two composite system reflectivity data sets, each having a common unknown Cr/Au and lipid multilayer component. However, one composite system had a silicon substrate as reference, whereas the other had a substrate of Al_2O_3 [90]. The SLD profile was obtained by direct inversion. First, the real part of the reflection amplitude, $\Re e(r)$, corresponding to the multilayer alone was determined algebraically, independently at each and every Q_z value of the two composite reflectivity data sets. This $\Re e(r)$ for the membrane possesses a one-to-one correspondence with a single nSLD profile. The direct inversion of $\Re e(r)$ yields the corresponding nSLD profile independent of any model and without any adjustable parameters, that is, it was retrieved ab initio. The profile obtained by this inversion is unique to the extent allowed by the truncation of the reflectivity data at Q_z^{max} and the degree of statistical uncertainty in the collected data. For comparison, Figure 3.5 also shows the nSLD profile predicted for this system by a MD simulation.

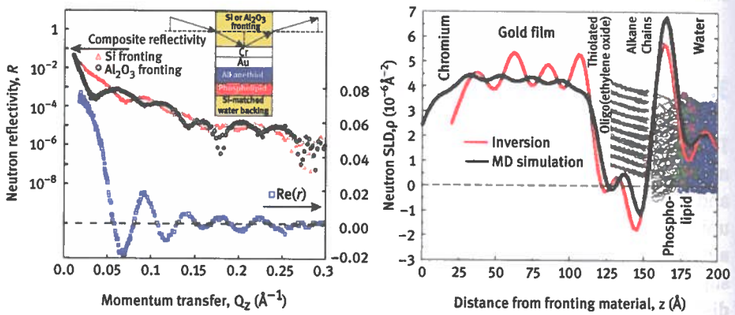

Figure 3.5: An example of direct inversion whereby the nSLD profile was extracted from two composite system reflectivity data sets, shown on the left, each containing a common unknown Cr/Au and lipid multilayer component, but each on a different reference substrate with known scattering properties. $\Re e(r)$ for the multilayer system alone, extracted from the two composite system reflectivity data sets, is also plotted. The direct inversion of $\Re e(r)$ yields the corresponding nSLD profile shown on the right, independent of any model and without any adjustable parameters. The oscillations are an artifact of the truncation of the composite system reflectivity data at Q_z^{max}. For comparison, the nSLD predicted for this system by a MD simulation is also shown. (Figure adapted from Majkrzak et al. [90].)

3.3 Planning a neutron reflectometry experiment

To determine the structure of a particular lipid membrane–protein complex with NR, the experimenter must identify a suitable model membrane system and experimental conditions – the aqueous membrane environment, bilayer composition and optimized protocol for protein addition – that in combination yield stably bound protein at sufficiently high interfacial density. Complementary surface sensitive techniques aid the characterization of the system of interest and are indispensable tools to optimize experimental conditions for structural characterization. In this section, we discuss in detail sparsely tethered lipid bilayer membranes (stBLMs) optimized for NR and two complementary surface-sensitive techniques for sample precharacterization: electrochemical impedance spectroscopy (EIS) [66, 93, 94] and surface plasmon resonance (SPR) [45, 95].

3.3.1 Sparsely tethered lipid membranes

Lipid bilayer membranes for biological applications of NR must meet several criteria that exclude investigations of natural membranes in vivo, but analogous studies can be performed using model membranes [63, 73, 96, 97]. For the best experimental resolution, the model membrane must be planar and of low interfacial roughness [86]. The relatively low flux at current neutron sources requires long NR measurement times, typically several hours per condition. The membrane must, therefore, be long-term stable. Large sample sizes of several cm^2 are advantageous as they allow for a larger incident beam cross-section and, therefore, higher flux on the sample. To ensure proper analysis of the NR data, the sample must be as homogenous in-plane as possible. Bilayers that are inhomogeneous, even on length scales below the coherence length of the neutron (see Section 3.2.2), require more complex modeling and lower the confidence with which structural features can be determined. Membrane defects in the interfacial bilayer may present nucleation points for nonspecific protein interactions that obstruct structural characterization of the biomimetic protein–membrane complex. Further, the interfacial bilayer should be representative of a lipid membrane in vivo, and be accessible for buffer exchange and protein addition in a series of NR measurements. As such, the model membrane system needs to be flexible in terms of its lipid composition and maintain lipid diffusion rates comparable to those of biological membranes. Finally, to focus on the structural changes induced by protein association with the membrane, the interfacial bilayer should be structurally inert with regard to changes in environmental conditions such as pH, temperature, and ionic strength.

A variety of model membranes have been developed for NR with those criteria in mind. A widely used platform is Langmuir monolayers, which are monomolecular films that resemble one leaflet of a lipid bilayer floating on a fluid (aqueous) surface. Proteins bound to Langmuir monolayers have been extensively studied with X-ray [98–100] and

neutron reflection [101–103]. X-ray reflectivity measurements in particular have a large accessible momentum transfer range [104], and consequently high resolution. However, Langmuir monolayers are fragile, making it difficult to inject proteins into the subphase without distorting the model membrane, and measurements usually require large amounts of protein because of large aqueous volume underneath the lipid layer.

A different class of experimental model systems suited for reflectometry investigations are double-layer lipid membranes supported by planar solid substrates – typically silicon wafers – either prepared as membrane stacks in a controlled humidity environment or as fluid-immersed single bilayers. Stacked membranes provide the advantage of periodicity, resulting in reflected intensities that form one-dimensional diffraction patterns [105, 106] with intrinsically higher spatial resolution than reflection experiments from single bilayers. In addition, increased sensitivity due to the large amount of membrane material in the sample permits the determination of in-plane structure and membrane fluctuations [107]. While stacked membranes can readily host peptides to reveal their association with lipids [108, 109], they are not well suited for the study of proteins, nor do these systems permit the in situ manipulation of protein–membrane complexes.

Fluid-immersed single lipid bilayer membranes on a solid support are arguably the most versatile class of model membrane systems for studying lipid-protein complexes with NR. This class includes purely solid-supported membranes [110, 111], hybrid membranes [112–115], tethered membranes [66, 93, 94, 116–119], polymer-cushioned membranes [120–124], and floating membranes [125, 126]. To keep bilayers on the solid support in-plane fluid, they can be deposited by various preparation protocols that create a nanometer-thin water layer or a molecular layer of a hydrated polymer between the membrane and the substrate.

We routinely use a hybrid of these two stabilization schemes in which an oligomeric, hydrophilic ethylene oxide ($EO_6 \ldots EO_9$) tether ligates the bilayer covalently to a gold-coated substrate to form a sparsely tethered lipid bilayer membrane (stBLM, see Figure 3.6) [59–61, 127, 128]. The tether provides ≈15 Å of hydrated submembrane space between bilayer and solid support. Spacing of the tethers is achieved by coadsorption with β-mercaptoethanol (βME), which also passivates exposed areas of the gold surface. While the narrow submembrane reservoir prevents studies of membrane proteins with large extra-membrane domains on both sides of the lipid bilayer, it ensures conformity of the membrane with the ultra-flat substrate, and thereby low interfacial roughness. stBLMs can be prepared virtually defect-free from a wide range of lipid mixtures. The high resilience of this model system [59, 129] permits the exchange of the adjacent buffer to make use of nSLD contrast variation (see Section 3.3.6) and to introduce or remove protein-containing solutions [52]. Complementary surface-sensitive techniques such as EIS [66, 93, 94] and SPR [45, 95] aid the characterization of the membrane systems and are indispensable tools to identify optimal conditions for structure determination by NR. The assessment of fluorescent probe dynamics within the membrane, for example by fluorescence correlation spectroscopy (FCS), confirms the in-plane fluidity of the model systems [130].

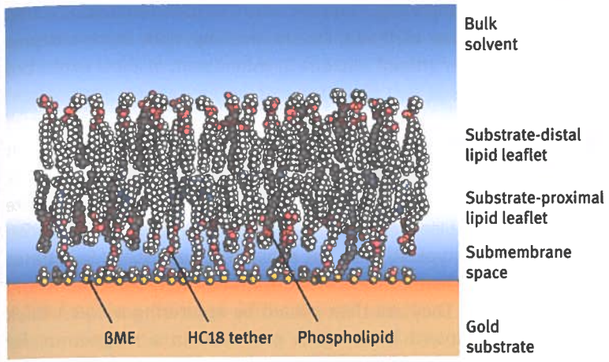

Figure 3.6: Cartoon of a sparsely tethered bilayer lipid membrane (stBLM) on a gold-coated support, composed of a tether lipid (designated as HC18 (Budvytyte et al. [61]); drawn with blue carbon atoms) that form membrane anchors for a POPC/POPS bilayer. Coadsorbed β-mercaptoethanol (βME) prevents the formation of a dense tether layer by occupying void substrate areas between tether molecules, thus passivating the gold surface. The ≈15 Å-thick water-filled submembrane space decouples the lipid bilayer membrane from the substrate and enables lipid diffusion in both lipid leaflets at a rate similar to that in giant unilamellar vesicles (Shenoy et al. [130]). The proximity of the membrane to the substrate quenches bilayer undulations, thus increasing the effective resolution with which bilayer components and bilayer-associated proteins can be resolved by NR.

3.3.2 Choosing a lipid composition

Synthetic model membranes reduce the chemical and functional complexity of cellular membranes such that a limited number of components still represent the molecular interactions that underlie a biological function of interest [96, 97]. In many cases, it is the selective interaction of a particular protein with the membrane and its specific organization in the lipidic environment that holds the key for understanding its function in a complex machinery. A first step is then to identify the cellular target membrane for the protein of interest. Since each of the internal membranes that form the boundaries of organelles or of the cell itself is composed of a unique mixture of phospholipids, sphingolipids, and sterols, the composition of the target membrane is an important feature to reproduce when designing a model membrane [131, 132]. Common molecular mechanisms for targeting peripheral proteins to membranes include electrostatic attraction to charged lipids, biochemical specificity to lipids such as phosphoinositides, and hydrophobic interactions via protein lipidation, for example, through posttranslational fatty acid or isoprenyl ligations – or a mix of all of the above [133]. To characterize the interactions that drive binding and find a

lipid composition of optimal complexity, it can be useful to probe each interaction individually using only a subset of lipids, before working with more complex mixtures [95].

3.3.3 Preparation of sparsely tethered lipid membranes

NR investigations require large, flat and atomically smooth substrates to maximize resolution and the signal-to-noise ratio in a measurement. Gold-coated silicon wafers of 2″ or 3″ diameter are typically used as substrates for stBLMs. Substrates are cleaned in sulfuric acid for 15 min, rinsed with ultrapure water and ethanol, and dried in a stream of nitrogen. They are then coated by sputtering a ≈ 40 Å-thick chromium adhesion layer followed by a ≈150 Å gold film in a magnetron. By optimizing the sputtering process, a root mean square roughness of <5 Å can be routinely achieved on silicon wafers polished to a surface roughness <3 Å, as confirmed by atomic force microscopy or X-ray reflection. The most critical parameter during deposition to achieve a low surface roughness is the pressure of the sputter gas, which should be <1 mTorr. Deposition power and voltage are parameters that require additional optimization. After sputtering, the substrates can be vacuum-sealed and kept for several days until use. Optimal gold layer thicknesses for complementary characterization techniques are ≈ 450 Å for SPR, and ≈ 2,000 Å for EIS. SPR and EIS have more relaxed requirements on surface roughness and require sample areas of 1 cm^2 or less. Therefore, glass slides can be conveniently used instead of silicon wafers. Due to the sensitivity of EIS with respect to even a small number of membrane defects, it is advisable to form stBLMs immediately after gold deposition for this technique.

The lipid composition of the membrane has to be matched with one of the available stBLM tether chemistries [59–61, 127, 128]. In our experience, biomimetic lipid membranes with unsaturated lipids are best supported by the HC18 tether, which has an EO_6 spacer between the terminal thiol and a glycerol backbone that branches into two unsaturated oleoyl chains [61]. Gold-coated substrates are then incubated in an ethanolic solution of a thiol-terminated tether lipid and βME, typically at a molar ratio of 30:70 and a total concentration of 0.2 mM. Upon incubation, the organic molecules form a self-assembled monolayer (SAM) via thiol bonds to the gold surface, and the ratio of tether lipid and βME controls the tether surface density. However, the ability to form insulating, defect-free lipid bilayer membranes is impaired if the tether density falls below a certain threshold, and a 30:70 (tether lipid:βME) ratio constitutes a compromise between low tether density and membrane integrity [59].

A standard technique for completing the stBLM after SAM formation is rapid solvent exchange (RSE) [59, 134]. Here, the SAM of tether molecules and βME is exposed to a ≈ 10 mg/mL solution of lipids in organic solvent. Most zwitterionic lipids readily dissolve in ethanol, whereas anionic lipids require more polar solvents such as mixtures of methanol and chloroform with small amounts of water. The RSE technique leads to membranes of superior quality with standard lipids [59] but may lead to poor results with mixtures of lipids that have significantly different solvent requirements [60]. Vesicle fusion is an alternative that provides better results for lipid mixtures. To aid the formation of defect-free bilayers via vesicle fusion, osmotic shock can assist membrane completion [135, 136]. A standard protocol involves mixing the lipids at the desired molar ratios in chloroform, then evaporating the solvent under vacuum for 12 h. The dried lipid films are re-hydrated in aqueous buffer or pure water with 1–2 M NaCl to a lipid concentration of 5 mg/mL, sonicated until clear, and allowed to incubate the SAM for 1 h. Thereafter, the vesicle solution is slowly replaced by a low salt buffer (50 mM NaCl) to promote vesicle rupture and bilayer completion, followed by a vigorous rinse to remove any remaining vesicles from the bilayer surface. Parameters in this generic procedure that can be optimized for a particular lipid composition are ionic strength, vesicle size, vesicle concentration, temperature, and buffer pH [135].

3.3.4 Assessing membrane quality

Defect-free lipid membranes are a prerequisite for a successful structure determination of membrane-associated proteins with NR. However, the size of membrane defects often is below the resolution limit of direct imaging techniques such as fluorescence microscopy or atomic force microscopy [94, 137]. Therefore, the propensity of a desired lipid composition for forming complete lipid membranes of low defect-density is most easily quantified by measuring the electrical properties of the membrane. On solid substrates such as those used for stBLMs, EIS is an ideal tool to assess bilayer quality [59, 94, 117] and is also well suited to monitor the effect of protein adsorption on membrane integrity [66, 93]. EIS measures the impedance of the membrane as a function of alternating current (AC) frequency [138], from which the density and size distribution of membrane defects can be determined [94, 139]. To characterize stBLMs, a three-electrode configuration is typically used: the gold coated substrate serves as the working electrode, a saturated silver-silver chloride reference electrode is placed in solution on the opposite side of the membrane, and a 0.25-mm-diameter platinum wire coiled around the barrel of the reference acts as an auxiliary electrode. Equivalent circuit models (ECMs) describe the electrochemical system in terms of circuit components and are used to extract physical parameters of the sample from the EI spectra.

Figure 3.7 shows a typical EIS spectrum of a stBLM represented as a Cole-Cole plot (real part vs imaginary part of the complex capacitance $C = (2\pi jfZ)^{-1}$,

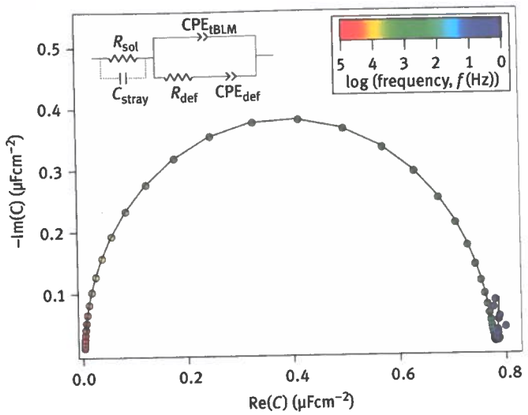

Figure 3.7: Cole–Cole plot of the electrochemical impedance spectra of a stBLM with a complex lipid mixture (30 mol% POPE, 19.5 mol% POPC, 0.5 mol% DMPC, 20 mol% POPS, 30 mol% cholesterol). The solid black line is the best-fit to a model defined by the equivalent circuit shown in the inset. The capacitance of the bilayer is $C_{tBLM} \approx 0.79\ \mu Fcm^{-2}$ (purely capacitive CPE, $\alpha = 1$) and the bilayer resistance is $R_{def} \approx 2\ M\Omega cm^2$.

where f is the AC excitation frequency and Z is the complex impedance). The combined capacitance of the membrane and Helmholtz layer dominates the semicircular shape of the spectrum. The membrane capacitance, inversely related to the thickness of the interfacial film, is approximately equal to the semicircle diameter. The example shown here represents a high-quality bilayer with low defect density. Signatures of membrane defects will show in the low-frequency region of the spectrum at the right-hand side of the figure: the minimum of the curve is a measure of DC defect current (i.e., the curve approaches the $\Re e(C)$ axis closely for highly resistant bilayers); a low-frequency tail develops beyond the minimum (blue-magenta points in the plot) for defective membranes. In membranes that incorporate protein pores, this tail can easily become larger than the semicircle that represents the membrane capacitance.

The solid line is the calculated impedance of the ECM shown in the inset of Figure 3.7 after fitting to the experimental data. This model uses two constant phase elements (CPEs), defined through their impedance $Z_{CPE} = Q_{CPE}/(j\omega)^{\alpha}$ to describe the electrical properties of the bilayer and its defects. Q_{CPE} is the CPE coefficient, measured in (farad $cm^{-2}\,s^{\alpha-1}$). The CPE exponent α can vary between 0 (purely resistive) and 1 (purely capacitive) and is typically close to 1 for the unperturbed bilayer in the measured frequency range, as expected for a nonconducting capacitor. In distinction, the CPE exponent for defect areas is close to 0.5, due to ion mobility limitations in the submembrane space and, therefore, a frequency dependence of the relaxation

of the potential across the bilayer via ion current through the defects. Such a frequency-dependent impedance is frequently encountered at electrode surfaces as well [94]. The other ECM elements account for the solution resistance R_{sol}, capacitances associated with the measurement setup, C_{stray}, and the frequency-independent resistance of bilayer defects.

3.3.5 Quantification of protein binding to the membrane

Measuring membrane-binding affinities is an essential prerequisite for NR measurements, in particular for peripheral membrane proteins. The lipid composition of the membrane and buffer conditions are the most frequently optimized parameters of the model membrane system with respect to binding affinity, affecting the protein concentration to which a membrane needs to be exposed during an NR experiment. Currently, NR requires 5–10% protein volume occupancy at the membrane to reliably determine the structural profile of a protein–membrane complex. Not in all cases, this coverage can be achieved under conditions that mimic the situation *in vivo*. Whether the binding affinity under physiological conditions is indeed too weak to achieve a sufficient surface coverage for NR, or whether the knowledge about the *in vivo* system is insufficient can often not be determined. As a consequence, a protein's binding affinity is often increased by expanding the fraction of lipids in the membrane that promote a particular binding mechanism. An increased anionic lipid content, for example, will enhance electrostatic interactions of a basic protein with the membrane. Optimizing the ionic strength of the aqueous buffer is another way of tuning this particular interaction, as long as this does not affect protein solubility. In such optimization, often a balance has to be achieved between mimicking *in vivo* conditions and achieving optimal conditions for structure determination. In addition, peripheral membrane proteins often adopt distinct binding conformations under different environmental conditions, which significantly complicate this optimization process [46] but may also provide valuable mechanistic insight.

Membrane affinities of proteins can be measured with direct or indirect assays. In direct assays, the protein–membrane interaction is continuously monitored, while indirect assays physically separate and then quantify membrane-bound and free protein fractions. These assays employ a variety of model membranes such as unilamellar vesicles, membranes tethered to solid supports and free-standing planar bilayers. Indirect assays often invoke centrifugation and chromatographic separation methods [140] while direct quantification methods frequently utilize intrinsic fluorescence or resonance energy transfer assays, isothermal titration calorimetry [140], quartz crystal microbalance with dissipation (QCM/D) [141, 142], bilayer overtone analysis [56], and SPR [56, 140, 143, 144]. The advantages and disadvantages of each method will not be discussed here, but methods that utilize planar supported bilayers

are well-suited for a direct application to NR experiments. SPR is one such method and it is routinely applied to measure protein binding to stBLMs.

SPR is an optical technique, sensitive to refractive index changes near a metal–solute interface, used to measure the membrane association of biomolecules in real-time [144]. A common optical setup, the Kretschmann configuration [145], is shown in Figure 3.8. Collective oscillations of free electrons (surface plasmons) are excited at the metal–solute interface under a narrow range of optical conditions. When polarized light strikes the metal film under total internal reflection, and energy and in-plane momentum of the incident monochromatic light simultaneously match that of the surface plasmon mode, photons are converted into surface plasmons [143]. This occurs at a specific angle of incidence, the resonance angle, and is observed as a reduction in the intensity of the reflected beam. When the refractive index near the metal–solute interface changes as protein binds to the membrane, the resonance angle changes. This shift is monitored as a function of time over a range of protein solution concentrations. Equilibrium values of the resonance angle for each protein concentration yield the binding curve from which thermodynamic parameters, such as the equilibrium dissociation constant K_d and the saturation SPR response, can be determined (see Figure 3.8).

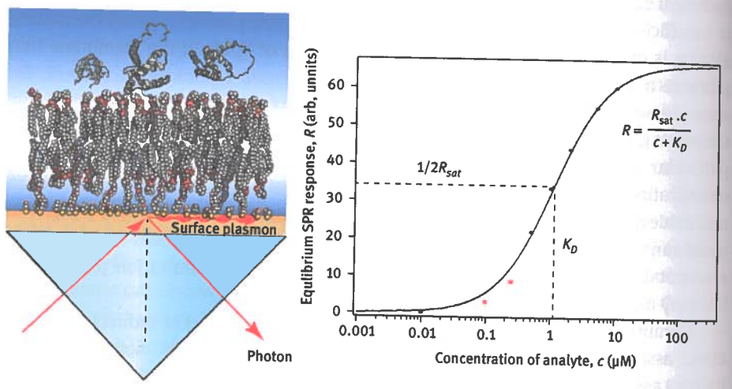

Figure 3.8: Left: Surface plasmon resonance in the Kretschmann configuration for the characterization of protein binding to an stBLM on a gold film. Surface plasmons at the metal–solute interface are excited by incident polarized light under conditions of total internal reflection. The resonance angle at which the conversion occurs (SPR response, R) depends on the refractive index of the material at the metal–solute interface and is monitored as a function of protein concentration in the solute. Shifts in resonance angle are proportional to a change in the amount of membrane-associated protein. Right: Binding curve modeled with a Langmuir isotherm. The Langmuir model yields the dissociation constant K_D of the binding process which is related to the free energy of binding per protein. K_D has the units of a concentration and represents the protein concentration at which one half of the membrane surface sites are occupied by protein (one half of the saturation response R_{sat}).

A standard model for analyzing protein–membrane binding is the Langmuir adsorption model [146]. It assumes a single-step binding event of a ligand (protein) to a receptor (membrane surface site). Each surface site typically contains several lipid molecules.

$$P + \mathrm{Mem} \underset{k_{off}}{\overset{k_{on}}{\rightleftharpoons}} P\mathrm{Mem}$$

In this kinetic representation of the Langmuir model, the dissociation constant is defined by the ratio of the rate constants of the association and dissociation processes at equilibrium, $K_D = k_{on}/k_{off}$. K_D is also directly related to the free energy of binding $\Delta G = RT \ln(K_D/c^o)$, in which R is the ideal gas constant, T is the temperature, and c^o the standard reference concentration. The Langmuir model does not account for protein–protein interactions in solution or at the membrane, nor does it take into account contributions to the free energy of binding from lipid reorganization or protein crowding at the membrane. Advanced models consider more complex scenarios such as multistate binding events in which conformational changes of the protein occur following membrane binding [146–153].

3.3.6 Optimizing the scattering length density contrast by sample deuteration

The ability to isotopically label, and thus highlight, parts of the interfacial structure is an advantage of neutron scattering that allows specific substructures to be distinguished from other sample components [154]. The exchange of protium for deuterium in biological structures enables large changes in the nSLD of sample components because the scattering cross-sections of ^{1}H and ^{2}H are extremely different, and hydrogen atoms are ubiquitous in biological matter. Therefore, ^{1}H/^{2}H exchange is the most facile and most frequently utilized method to create contrast for neutron scattering in biological samples. There are three major strategies of taking advantage of isotopic labeling in NR from membranes and membrane-bound proteins. Most easily, variation of the bulk solvent nSLD provides scattering contrast, in particular for solvent-containing elements of the interfacial structure (see Figure 3.9). Second, isotopic labeling of a particular protein or specific regions in a protein highlights those regions with respect to its molecular surrounding. This is particularly useful for resolving the structure of protein complexes at the membrane. Finally, lipid deuteration can be used to tune the contrast between the lipid membrane and embedded molecules, such as proteins with trans-membrane domains.

Finding the best deuteration scheme is an optimization problem that requires experience and computational strategies. It is generally good practice to simulate NR data based on anticipated experimental outcomes to assess the sensitivity of the experiment toward the structural features of interest, and it is convenient to combine this exercise with a systematic exploration of deuteration schemes. The use of advanced methods such as the calculation of the information content of the reflectivity data anticipated from different experimental setups puts this optimization process on a quantitative footing [155].

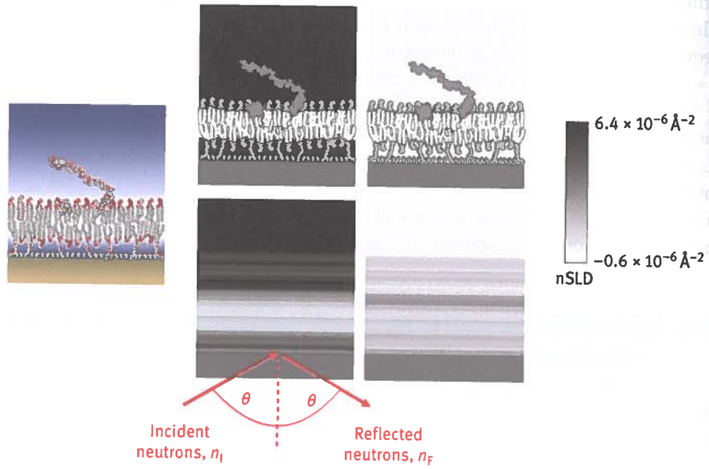

Figure 3.9: Bulk solvent contrast in two related NR experiments highlights different structural features of the surface architecture. Subsequent measurements of the same sample with bulk solvents of different nSLD and simultaneous analysis of all measured contrasts constrains model parameters strongly and increases the confidence, in particular in regions that contain solvent. Left: The colored cartoon shows the structure of a tethered membrane composed of a lipid bilayer and associated protein (α-synuclein (from Jiang et al. [156])). Center and Right: The grayscale images visualize the same cartoon with color-coded nSLD (center: D_2O-based bulk solvent (nSLD = 6.34 × 10^{-6} Å^{-2}), right: H_2O-based bulk solvent (nSLD = −0.56 × 10^{-6} Å^{-2})). The bottom row shows the in-plane averaged nSLD profiles that give rise to two distinct reflectivity curves. The directions of the incident and reflected neutron beam relative to the sample orientation are indicated in red.

3.4 Conducting the neutron reflectometry experiment

Figure 3.10 shows a schematic view of a typical neutron reflectometer located at a reactor neutron source where a single-crystal monochromator is used to obtain a quasi-monochromatic beam of neutrons. In contrast, reflectometers at pulsed neutron sources distinguish neutrons of different wavelengths via time-of-flight methods, but collect essentially the same reflectivity data as a function of Q_z. Included in the instrument diagram of Figure 3.10 are polarizing and spin flipping devices for measurements utilizing polarized neutrons (the neutron is a Fermion with spin 1/2). The use of polarized neutron beams, particularly in the study of magnetic materials, is reviewed in ref [157]. Polarized neutron beams are of relevance for NR studies of nonmagnetic materials when magnetic reference layers are used for phase-sensitive measurements. In this section, we discuss some of the practical considerations involved in carrying out NR measurements.

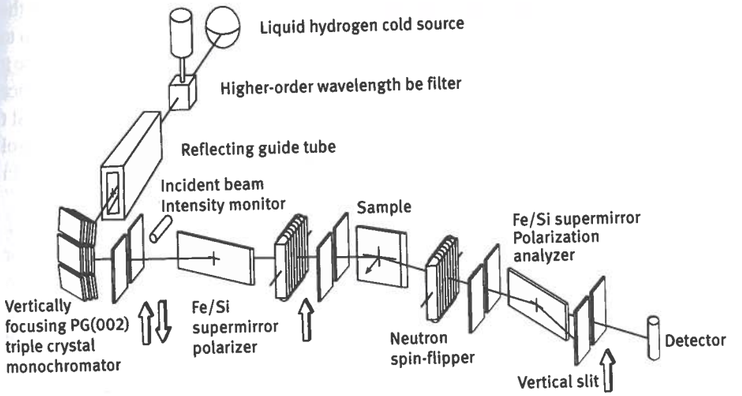

Figure 3.10: Schematic illustration of a typical neutron reflectometer at a reactor source. Thermal neutrons from the reactor core are moderated in the liquid hydrogen cold source to obtain a beam with wavelengths larger than 2 Å. A Be filter eliminates neutrons with a wavelength below 4 Å. A single wavelength of typically 5 Å is selected by a pyrolytic graphite triple crystal monochromator via Bragg reflection and diverted into the instrument at an angle of ≈ 90°. A pair of presample apertures defines the neutron beam incident on the sample whose intensity is determined in a beam monitor. A pair of postsample apertures reduce background scattering at the detector position while allowing the specularly reflected beam to be registered in the detector. The angle of incidence and the scattering angle can be independently varied. Included in the schematic are polarizing and spin-flipping devices used with polarized beams if the sample contains magnetic reference structures.

3.4.1 Data acquisition and instrumental resolution

Independent from whether a reflectometer uses a monochromatic neutron beam (see Figure 3.10) or whether neutrons of a range of wavelengths are incident on the sample, data collection typically involves measuring the specular reflectivity (see Section 3.2.2), additional nonspecular neutron intensities from which the background contained in the specular signal can be determined, and the incident beam intensity for every instrument configuration used during the measurement. Obtaining a single reflectivity curve for data analysis from this set of raw NR data is called data reduction. It typically involves the subtraction of the background from the specular signal and the division of the background-corrected specular signal by the incident beam intensity. Details vary for different instruments. Scattering facilities often provide remote online data reduction and analysis services that allow for immediate data processing during the measurement [158]. This is particularly useful for NR studies of systems such as those discussed here, as the accuracy of the measurement is a key factor for a successful protein structure determination and remote data reduction software allows for an early assessment of all separately measured raw data.

To obtain accurate SLD depth profiles from specular NR data, it is essential that the measurement is performed with commensurate precision and accuracy. It is common to measure the reflectivity with uncertainties as low as a fraction of a percentage. To do so it requires that systematic errors be minimized by proper alignment of the reflecting surface of the sample relative to the incident beam, exact definition and calibration of slit apertures, and proper compensation of backlash in gear drive mechanisms that control rotation angles. Proper accounting for the propagation of systematic uncertainties in signal, background, and incident beam intensity measurements is necessary as well.

As discussed in Section 3.2.1, each individual neutron wave packet has a coherent distribution of component basis states, each with a different wave vector $\boldsymbol{k}_j$ and a mean wave vector $\boldsymbol{k}_M$. Therefore, the beam of independent packets has an incoherent distribution of these mean wave vectors, specified by their angular divergence as well as (a narrow) distribution of wavelengths. A measured reflectivity curve, $R(Q_z) = |r_{\text{meas}}(Q_z)|^2$, is then a convolution of the actual reflectivity of the sample, $|r_{\text{sample}}(Q_z)|^2$, and the instrumental resolution characterized by the effective ΔQ associated with the beam angular divergence and wavelength spread. For monochromatic reflectometers at reactor sources, $\Delta\lambda/\lambda$ is typically of the order of 1–5% and $\Delta\theta$ is of the order of a few minutes of arc.

3.4.2 Low-background fluids sample cells

The ability of neutrons to be transmitted through long distances with negligible scattering or absorption loss in certain materials such as single-crystal silicon makes

it possible to measure the reflectivity from lipid membranes on solid substrates adjacent to fluid aqueous reservoirs. NR experiments of membrane-associated proteins on stBLMs typically utilize a fluids cell that allows for in situ buffer exchange (see Figure 3.11) [90]. This enables the study of the evolution of the interfacial structure after addition of small molecules or proteins, or after changing the ionic strength, pH, or temperature of the bulk solvent. Each such condition is typically measured using two isotopically distinct bulk solvents, for example H_2O and D_2O-based buffers (see Section 3.3.6). To verify that the sample is not changing during the measurement of any of those sequential conditions, every individual reflectivity measurement consists of two scans over the entire Q_z-range that can be later combined.

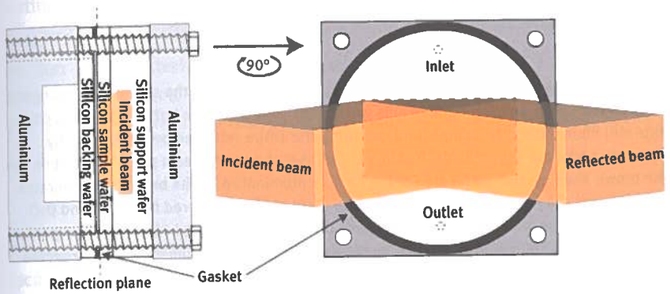

Figure 3.11: The NCNR fluids sample cell for NR measurements. Left: The fluids cell consists of a stack of three 3″ diameter silicon wafers clamped into an aluminum frame that can be mounted at the sample position of the NR instrument. A supported membrane is prepared on a 5–mm-thick Si wafer ("sample wafer") that faces a ≈ 100–µm-thick exchangeable aqueous reservoir (blue layer) defined by a Viton gasket (black). Right: View from the sample wafer facing the aqueous reservoir. The fluid inlet and outlet are drilled into the backing wafer. The footprint of the incident beam on the sample wafer is kept constant during the NR measurement by progressively opening the beam-defining slit apertures as the incident angle θ increases. Note that the incident and reflected neutron beams (orange) traverse macroscopic distances in the 20 mm thick Si "fronting" support wafer and the sample wafer with small attenuation. The refractive bending of the beam upon entry to and exit from the rectangular Si crystal support (Majkrzak et al. [30], Maranville et al. [159]) is not shown. Numerical data reduction and fitting programs perform the appropriate corrections (Kirby et al. [38], Maranville [158]).

The main limitation to the accessible Q_z-range of a neutron measurement using a fluids cell, and thus, the main limitation on the spatial resolution of the experiment, is the amount of background scattering originating from the sample. Therefore, in the remainder of this section, strategies to minimize this scattering are discussed. The beam geometry at the fluids cell sample position of an instrument such as that shown in Figure 3.10 is presented in Figure 3.12a. The monochromatic neutron beam is

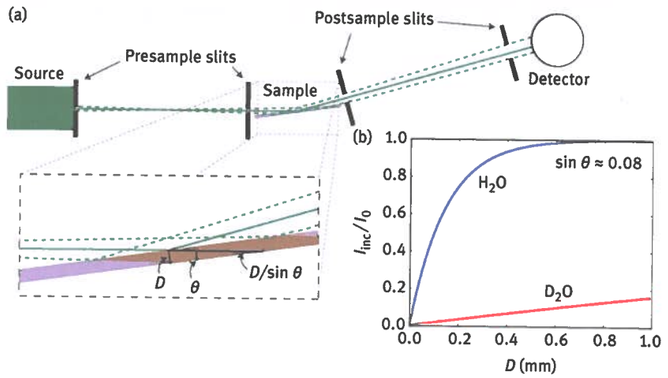

Figure 3.12: Design considerations for an NR experiment. (a) Schematic of the sample geometry at a neutron reflectometer. Pre- and postsample slits are chosen to provide the tightest possible collimation while still illuminating the sample and capturing the entire reflected beam. Maximally divergent neutron paths are shown as dashed lines. The inset shows the beam paths incident on the sample; the brown shading shows the area of the sample illuminated by the beam that generates isotropic background. (b) Fraction of incident intensity incoherently scattered from H_2O and D_2O sample reservoirs as a function of reservoir thickness D shown in the inset in (a). Multiplying this fraction by the fractional solid angle observed by the detector gives an estimate for the expected background (incident angle 4.56°, $Q_z = 0.2$ Å^{-1} for 5 Å neutrons; $\sin\theta \approx 0.08$).

collimated by two presample slits. Background scattering arises primarily from isotropic incoherent scattering from the liquid in the sample cell. Therefore, minimizing the volume of liquid that is both illuminated by the beam and observed by the detector is the most direct approach for background reduction. This requires the narrowest possible (most highly collimated) incident and reflected beams. A ratio of the presample slit openings of 1:1 is optimal, with the value of the slit opening chosen in an angle-dependent manner to illuminate the same total area of the sample over the entire Q_z-range. Two postsample slit openings are chosen to admit the entire reflected specular beam while admitting a minimum of ancillary scattering.

For membrane protein structure determination, a typical number of (nonbackground) neutrons observed in a single NR spectrum with $Q_z^{max} = 0.25$ Å^{-1} are 200,000. The counting time required to observe this number of neutrons varies considerably with the source intensity but is usually several hours. To improve the measurement speed, a divergent beam can also be utilized, where the first presample slit is open wider than the second presample slit. This configuration increases the incident flux on the sample, decreasing count times but increasing the background observed by the detector, and reduces the angular resolution of the measurement. Optimal slit conditions are often chosen to balance experiment speed and background reduction.

The liquid reservoir dimensions of the fluids cell are chosen to minimize the background generated by isotropic incoherent scattering. Neglecting scattering from the cell support materials, a simple estimate of the background level as a fraction of the incident intensity for a given flow cell design is as follows. A beam scattered by the liquid reservoir of thickness D at an angle of incidence θ has a path length through the material $D/\sin\theta$ (see Figure 3.12a). The incoherently scattered fraction of the incident beam is given by:

$$\frac{I_{inc}}{I_0} = 1 - e^{-\frac{\epsilon D}{\sin\theta}}$$

Here, ϵ is a materials property of the reservoir liquid representing the inverse extinction length from incoherent scattering. For 5 Å neutrons incident on D_2O, $\epsilon_{D_2O} = (72.2\,\text{mm})^{-1}$; for H_2O, in which hydrogen has a much larger incoherent cross-section than deuterium, $\epsilon_{H_2O} = (1.84\,\text{mm})^{-1}$ [83]. In Figure 3.12b, the background level is plotted as a function of reservoir thickness for an incident angle of 4.56°. The actual background observed in a measurement is approximated by:

$$\frac{I_{bkg}}{I_0} \approx \frac{\Omega_d I_{inc}}{I_0}$$

where $\Omega_d \approx A_d/4\pi L_{ds}^2$, the fractional solid angle subtended by a detector of area A_d located a distance L_{ds} from the sample, is typically ~10^{-5}.

From Figure 3.12b, it is inferred that an optimal signal-to-noise ratio requires the reservoir thickness to be even smaller than 100 µm. In addition, if the Si support media that surrounds the sample and the reservoir can be decreased to thicknesses of ½ mm or less, inelastic contributions to the background scattering from Si are diminished. It has been shown that such a combination of improvements in sample cell design that minimizes incoherent scattering from both the buffer and the sample support structure allows measurements of reflectivities as low as 10^{-8} at $Q_z^{max} = 0.7$ Å^{-1} [113]. In practice, it remains difficult to routinely prepare such thin samples and mechanically stabilize them during the measurement.

3.4.3 Measuring membrane-associated proteins

Sample preparation, in particular that of stBLMs, is detailed in Section 3.3.3. The last step in this procedure, lipid bilayer completion by osmotic shock-aided vesicle fusion, is typically carried out directly in the fluids cell (see Section 3.4.2). After bilayer completion, the cell is mounted and aligned at the sample stage of the NR instrument. Data are typically collected for the as-prepared bilayer first, using at least two isotopically distinct bulk solvents, such as H_2O- and D_2O-based buffer. A buffer exchange is accomplished by flushing the cell with at least six times its volume. A

complete set of reflectivity data consists of measurements of the specular reflection and the scattering background over the entire range of incident angles, as well as a beam-normalization scan that determines the intensity of the incident neutron beam at every angle. Details of those measurements vary between different instruments.

Before adding protein to the sample and at the earliest opportunity, the NR data of the as-prepared lipid bilayer should be analyzed. A structural characterization of a membrane-bound protein at the highest possible resolution requires a complete lipid bilayer, as bilayer defects at the very least complicate data analysis – if they do not lead to nonspecific protein association, which obliterates the determination of the biologically relevant protein–membrane complex structure altogether. As a rule of thumb, lipid bilayers that are less than 90% complete should be discarded, and the best data are obtained from bilayers that are well over 95% complete.

Preparing the protein for measurement is straightforward if the protein stock buffer already matches the desired experimental buffer. In this case, protein at the desired concentration is prepared by diluting an aliquot from the stock solution with the working buffer to the final concentration. If the buffers do not match, dialysis cassettes or spin columns are used for an exchange of the protein buffer. Dialysis is the gentler method but requires large volumes, which is often not cost-effective when exchanging into a D_2O-based buffer. After the buffer exchange, the protein concentration needs to be reassessed such that an aliquot from the new stock can be diluted with working buffer to achieve the desired concentration for the NR experiment based upon the independently determined protein dissociation constant K_D (see Section 3.3.5). A concentration moderately higher than the value of K_D is often a good compromise between sufficient protein coverage for structure determination and a too dense protein coverage that might lead to undesirable protein–protein interactions at the membrane. Thin reservoirs such as those used in NR sample cells can be depleted of protein by membrane binding. For a 100 µm reservoir, this typically occurs when protein binds to the membrane with high affinity ($K_D < 1\,\mu M$). Repeated injections of multiple cell volumes, or a continuous supply of protein, are then required to achieve an optimal protein surface coverage.

Different incubation protocols can be useful for measuring the structure of a membrane-associated protein: (1) The NR measurement is performed while protein is present in solution for the entire time of the measurement, which can be several hours. (2) The lipid membrane is incubated with protein for a set period based on binding kinetics observed with SPR and then replaced by pure buffer before the NR measurement is initiated. The choice between the two strategies is determined by factors such as the rate at which the protein dissociates from the membrane, and the long-term stability of the protein in solution. When an NR measurement takes place with protein in solution, it is useful to measure another set of reflectivity curves after rinsing with pure buffer. Differences of the interfacial structure before and after rinsing then indicate that a fraction of the membrane-bound protein assumes an alternate

conformation that dissociates fast from the membrane. A comparison of the measurements before and after buffer rinse can help delineate both protein structures [41].

Automation of buffer exchange reduces manual effort. Various pumping schemes are available for buffer exchange: syringe pumps inject premixed solutions and are convenient to use; peristaltic pumps are ideal for circulating flow and in situ dialysis procedures; and chromatography pumps and valves can be used to automate both mixing and flow. When using such devices, experimenters should be cognizant of the temperature requirements to maintain the stability of any protein-containing solutions. Protein adhesion to tubing walls and denaturation due to shear in microtubing are additional concerns.

3.5 Data analysis

As direct inversion of NR data from biomimetic systems to obtain the structural profile of the sample is in most cases not practical (see Section 3.2), data modeling becomes the prevalent data analysis strategy in biological NR. The ultimate goal of NR data modeling is to identify a parametric molecular model of the biomimetic interface that uniquely corresponds to the measured reflectivity. Intrinsically, NR only yields one-dimensional profiles of neutron scattering length densities along the interface normal while averaging in-plane within the coherence area of the neutron beam (see Section 3.2.2 and Figure 3.3) [30]. Since different materials in the interfacial architecture can have similar nSLDs, this profile may not be uniquely related to a structural profile. With the option of selective deuteration, however, it can usually be ascertained that the structural features of interest bear nSLDs sufficiently different from their immediate molecular surroundings and can, therefore, be resolved (see Section 3.3.6) [154].

NR data modeling makes use of the circumstance that the calculation of a unique reflectivity from a particular interfacial structure is possible, given that the nSLDs of all materials in the structure are known. A typical modeling strategy is then to iteratively find a realization of a suitably parameterized structural model that gives rise to the measured reflectivity. NR modeling is, therefore, a task of finding an appropriate model and a global solution within the parameter space of the model (see Figure 3.13). This procedure does not solve the missing phase problem, discussed in Section 3.2.3, however. Unique solutions are ensured by integrating additional information provided by bounds on model parameters, constraints on the model – such as volumetric data or the chemical connectivity of submolecular moieties – and multiple reflectivity measurements of isomorphic structures at distinct isotopic contrasts. The latter possibility is unique to neutron scattering and usually leads to very stringent constraints on the model when different sets of reflectivity data from one sample are corefined while sharing parameter values for immutable parts of the structure [38]. It has been demonstrated that such an integration of various sources

of information leads to unique solutions to the scattering problem [92], in particular, if an approximate structure is already known.

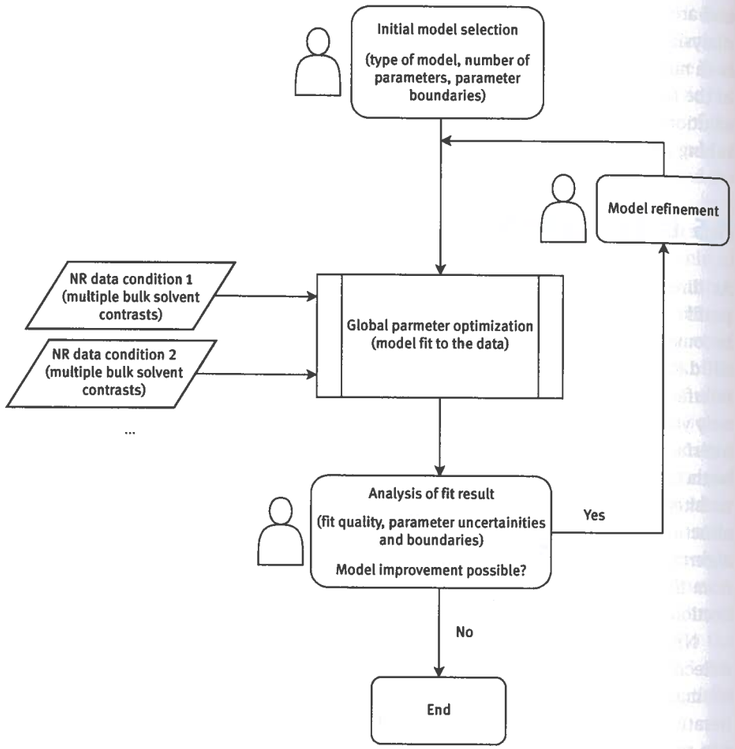

Figure 3.13: Flow chart of the iterative process underlying simultaneous modeling of multiple NR data sets. Steps that require user interaction because they are currently not automated are indicated. Global parameter optimization for the modeling of biomimetic systems requires a robust optimizer that searches the large parameter space efficiently. Solutions are often provided by implementing genetic algorithms (de Haan and Drijkoningen [160]) or a Monte Carlo Markov Chain-based optimizer (Kirby et al. [38], Braak [161], Braak, and Vrugt [162]).

Interfacial structures of proteins on bilayer membranes easily reach a degree of complexity that requires a large number of parameters in a realistic model. Therefore, rigorous methods are needed to determine parameter uncertainties that reveal over-

parameterization. We typically use a Monte Carlo Markov Chain (MCMC) global optimizer [38, 161, 162] that yields realistic parameter confidence intervals and provides access to full posterior parameter distributions from which parameter correlations can be identified. Such correlations are useful information for further model optimization. From the posterior, confidence limits on modeling results that are functions of multiple parameters, such as the area per lipid for a lipid bilayer or free-form spline profiles, can be readily calculated. The process of finding an adequately complex model supported by the data still requires empirical testing of models of various complexity (Figure 3.13), as algorithmic model selection [155, 163] has not yet been robustly implemented for NR. While each scattering facility provides software packages for NR data analysis to their beam users [38, 164–166], software modifications that support complex models for biomimetic systems are often required.

3.5.1 Composition-space modeling

A particularly powerful strategy for the analysis of NR data from biomimetic membrane systems is composition-space modeling (see Figure 3.14) [33, 64, 167]. This approach leads to component volume occupancy profiles along the bilayer normal that account for the solid substrate and spatial distributions of all molecular components of the interfacial architecture such as the lipid bilayer and membrane-associated protein. Each such distribution is associated with the scattering length of the particular component, which then allows for a facile computation of the nSLD profile of the entire structure that is needed for the calculation of the model reflectivity. The advantage of composition-space models over other approaches, such as conventional slab models [69], stems from a parameterization of the model that is directly tied to molecular structure. Furthermore, composition-space models readily integrate auxiliary information such as molecular volumes and chemical connectivity, which reduces the number of fit parameters and increases the confidence on unknown parts of the structure. As an example, volume occupancies of the headgroups in a stBLM are tied to their respective hydrocarbon chains since individual volumes for these two components are known from auxiliary methods such as X-ray diffraction [106]. Importantly, composition-space models allow for realistic representations of spatially overlapping molecular distributions, such as that of a protein that penetrates the lipid bilayer. Complete volume filling is achieved without overfilling the available volume or leaving void volumes in the structure. As a result, composition-space modeling has been successfully applied in a large number of studies [49, 58, 67, 95].

Volume occupancy profiles of components with unknown internal structures, such as a membrane-associated protein with unstructured regions, require representations by free-form models. Free-form Hermite splines can accurately describe arbitrary protein profiles (Figure 3.14) and join consistently with lipid bilayer profiles

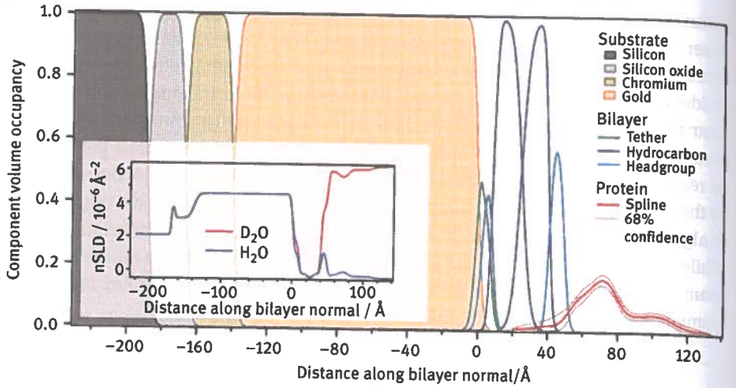

Figure 3.14: Schematic representation of a composition-space model that combines a traditional slab model for the substrate layers with a continuous distribution model for the lipid bilayer and an associated protein. The lipid bilayer is parameterized using volume occupancy distributions of its constituents (Shekhar et al. [64]) and the protein is modeled using a free-form Hermite spline (Heinrich and Lösche [33]). Volume not occupied by either substrate layers or molecular components is taken up by bulk solvent. The inset shows the nSLD profiles calculated from this model for H_2O and D_2O-based bulk solvent. In combination with similar profiles that fit NR data sets obtained for the as-prepared bilayer (not shown), the resulting general model restricts the parameter space so that the protein structure is determined with high confidence, as shown by the 68% confidence intervals associated with the red profile in the main panel.

to form protein–membrane complexes [33]. In this approach, the protein nSLD has a constant value, which is the average nSLD of the protein given its sequence. It accounts for partial deuteration due to proton exchange with D_2O- and H_2O-based buffers such that the protein nSLD values differ in isotopically distinct solvents. The number of control points that define the Hermite spline is determined by the spatial extension of the protein along the bilayer normal and iteratively refined. By allowing the control point positions to deviate from an equidistant separation, the flexibility of the Hermite spline is increased. Each control point, therefore, carries fit parameters for the volume occupancy of the protein envelope and the separation along the membrane normal. The MCMC optimizer discussed above is an essential tool to avoid over-parameterization as it provides an unbiased determination of the parameter uncertainties [38]. Volume occupancy profiles of constituents of protein–protein complexes at the membrane can be individually resolved if there is scattering contrast between them. This is most easily achieved by deuteration of one of the constituents. The model then includes two separately parameterized spline functions with different average nSLD values of its constituents [58].

3.5.2 Integrative modeling of interfacial structures

To obtain high resolution, three-dimensional information of membrane-bound proteins, integrative modeling strategies are required to supplement the NR data. NR data from surface-associated membrane proteins are routinely refined using crystallographic and NMR structural data within a rigid body modeling approach [33]. Within this approach, a volume occupancy protein profile and a scattering length profile of the high-resolution structure is obtained by projecting the solvent accessible volume and the coherent cross-sections [83] of all atoms of the protein onto the bilayer normal (see Figure 3.15). These two distributions are binned into microslabs of typically 0.5 Å thickness. The solvent accessible volume of the protein is calculated using Connolly's method [168, 169], but can also be derived from experimentally determined average volumes per amino acid, such as from SANS contrast-matching experiments [170]. Both profiles are then directly used within the composition-space model discussed above. The calculated volume occupancy profile can be freely placed at any distance along the bilayer normal (see Figure 3.14), thus allowing the

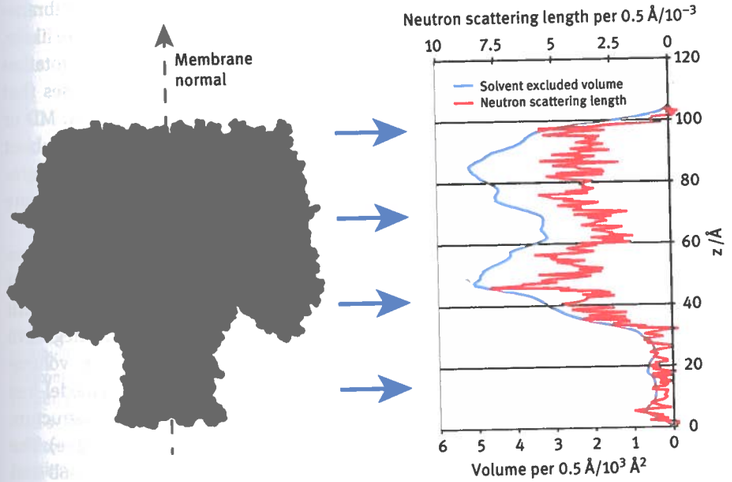

Figure 3.15: Projected, sliced solvent excluding volume and neutron scattering length profiles for the α-hemolysin membrane-pore (Brouette et al. [50]) based on the protein crystal structure (Song et al. [85]). The smooth volume profile was obtained by Connolly's method of rolling a sphere with the diameter of a water molecule over the protein's surface (Pattnaik [145]). The scattering length profile is a projection of discrete scattering centers onto the membrane normal and will be smoothed in successive steps of the data analysis with regard to thermal fluctuations of the atomic positions at room temperature.

protein to penetrate the lipid bilayer or to be strictly peripheral. The height of the protein profile can be scaled to represent different surface coverages. Different to the Hermite spline that is used for model-free protein profiles, the volume occupancy profiles derived from high-resolution structures have variable and potentially more accurate nSLD values associated with every position.

The rigid-body modeling approach underlies the assumption that the membrane-associated structure of the protein is not significantly different from the high-resolution structure. Under this condition, the position and orientation of the protein with respect to the lipid membrane can be determined with high accuracy [49, 66]. To determine the orientation of the protein, the high-resolution protein structure is rotated and projected in discrete steps of typically 5° about two of three Euler angles that are required to define a particular protein orientation. The third Euler angle is irrelevant since NR is invariant against rotational symmetry about the membrane normal [49]. All protein orientations are, thus, parameterized using two Euler angles that are optimized during NR data analysis using interpolation between the precalculated discrete orientations (see Figure 3.16c).

If no satisfactory fit to the data can be determined using a particular high-resolution structure, significant structural changes of the protein upon membrane-interaction, or significant rotational freedom of the rigid protein structure, are likely. A comparison of the volume occupancy profiles obtained from rigid body rotation and free-form modeling can pinpoint the underlying discrepancies. In cases that rigid-body modeling is not viable or ambiguities from the NR data remain, MD or Monte–Carlo simulations are powerful options to gain atomistic information about the membrane-bound protein. Several approaches utilize simulation-based integrative modeling [39, 49, 67, 171, 172], and efforts are underway to establish a complete integrative modeling framework for NR.

A recent example of integrative modeling is shown in Figure 3.16 and is illustrative of both the power and limitations of the technique [56]. The structure of cytoskeletal tubulin heterodimers on biomimetic mitochondrial membranes was interrogated with NR and optimized to the known high-resolution structure [173] using the integrative modeling procedure outlined in this section. The results are presented as volume occupancy profiles in Figure 3.16a and show good agreement between a model-free Hermite spline (black curve) and the profile calculated from a high-resolution structure after optimizing the protein orientation and bilayer penetration depth (red curve). The oriented high-resolution structure is shown in the upper panel of Figure 3.16b and corresponds well to a MD simulation of this system (lower panel). The rotation scheme and Euler angle definitions are shown in Figure 3.16c, while Figure 3.16d shows a probability plot of the tubulin orientation obtained from data analysis. Note, that while the orientation is well constrained in the tilt angle β (which changes the extension of the protein along the bilayer normal and is thus well constrained by NR), it is not as well constrained in rotation α around the heterodimer axis, because of the cylindrical shape of the protein. Likewise, Figure 3.16e shows a significant probability that the

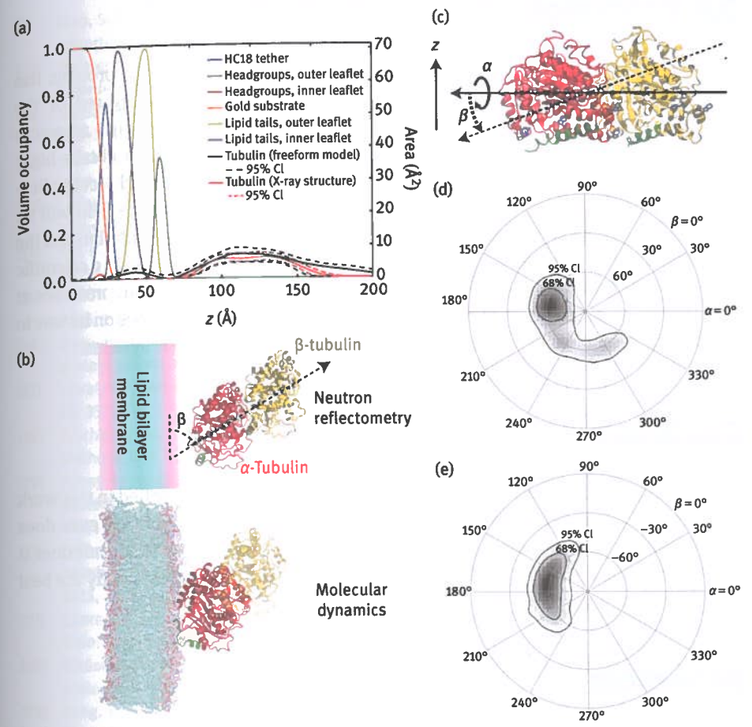

Figure 3.16: Orientation analysis of tubulin on biomimetic mitochondrial membranes. (a) Volume occupancy profiles of bilayer and protein, represented as a freeform model (black curve) and an atomistic model obtained by rigid-body rotation of the high-resolution structure (red curve). (b) Optimized structure of tubulin bound to the membrane through its α subunit obtained from NR (top) and MD simulation (bottom). (c) Definition of Euler rotations for the tubulin heterodimer. (d–e) Polar probability plots of tubulin orientations consistent with the NR data, in which tubulin is bound to the membrane through its α subunit (d) or β subunit (e). Due to the approximate symmetry of the low-resolution tubulin heterodimer structure, NR cannot distinguish between the two possibilities and is also not very sensitive to rotations about the heterodimer axis (Figure adapted from [56]).

tubulin heterodimer is inverted, that is, bound by the other component of the heterodimer. This example shows that NR is sensitive to transformations of a protein that are not about symmetry axes or planes, but cannot distinguish between configurations that produce similar low-resolution density profiles normal to the surface. In these cases, auxiliary techniques (in this example, MD simulations) are useful to distinguish among the structures allowed by the NR data.

3.6 Conclusion

NR from biomimetic lipid model membranes and membrane-associated proteins has seen tremendous improvements over the past decade. Those were triggered by the development of robust biomimetic model membrane systems and by major advances in NR data analysis. Using integrative modeling, it is now possible to obtain high-resolution structural information of membrane-bound proteins that finds direct application in biomedical research and biophysics. The immediate future of the field will be shaped by upcoming major improvements in neutron scattering instrumentation and the installation of new and more powerful neutron sources worldwide, increasing scientific throughput and allowing the field to expand into studying time-dependent processes at the membrane. Integrative modeling will further increase its footprint and is on its way to become the essential data analysis framework for NR from biomimetic systems.

Disclaimer

Certain commercial materials, equipment, and instruments are identified in this work to describe the experimental procedure as completely as possible. In no case does such an identification imply a recommendation or endorsement by NIST, nor does it imply that the materials, equipment, or instrument identified are necessarily the best available for the purpose.

References

[1] Alberts, B., Johnson, A., Lewis, J., et al. Molecular Biology of the Cell, 6 ed., Garland Science, Taylor & Francis Group, LLC, New York 2014, pp. 565–596.

[2] Heijne von, G. The membrane protein universe: what's out there and why bother? J. Intern. Med. 2007, 261, 543–557.

[3] Lodish, H.F., Berk, A., Zipursky, S.L., Matsudaira, P., Baltimore, D., & Darnell, J. Molecular Cell Biology, 4 ed., W.H. Freeman, New York 2000.

[4] van Geest, M., & Lolkema, J.S. Membrane topology and insertion of membrane proteins: search for topogenic signals. Microbiol. Mol. Biol. Rev. 2000, 64, 13–33.

[5] Nastou, K.C., Tsaousis, G.N., Kremizas, K.E., Litou, Z.I., & Hamodrakas, S.J. The human plasma membrane peripherome: visualization and analysis of interactions. Biomed. Res. Int. 2014, 2014, 397145–397112.

[6] Tatulian, S.A. Interfacial enzymes: membrane binding, orientation, membrane insertion, and activity. Methods Enzymol. 2017, 583, 197–230.

[7] Zielenski, J., & Tsui, L.C. Cystic fibrosis: genotypic and phenotypic variations. Annu. Rev. Genet. 1995, 29, 777–807.

[8] Jiang, M., Jia, L., Jiang, W., et al. Protein disregulation in red blood cell membranes of type 2 diabetic patients. Biochem. Biophys. Res. Commun. 2003, 309, 196–200.

[9] Xiao, S., & Shaw, R.M. Cardiomyocyte protein trafficking: relevance to heart disease and opportunities for therapeutic intervention. Trends Cardiovasc. Med. 2015, 25, 379–389.

[10] Meisler, M.H., & Kearney, J.A. Sodium channel mutations in epilepsy and other neurological disorders. J. Clin. Invest. 2005, 115, 2010–2017.

[11] Wymann, M.P., & Schneiter, R. Lipid signalling in disease. Nat. Rev. Mol. Cell. Biol. 2008, 9, 162–176.

[12] de Haan, L., & Hirst, T.R. Cholera toxin: a paradigm for multi-functional engagement of cellular mechanisms (Review). Mol. Membr. Biol. 2004, 21, 77–92.

[13] Ladokhin, A.S. pH-triggered conformational switching along the membrane insertion pathway of the diphtheria toxin T-Domain. Toxins (Basel). 2013, 5, 1362–1380.

[14] Yin, H., & Flynn, A.D. Drugging membrane protein interactions. Annu. Rev. Biomed. Eng. 2016, 18, 51–76.

[15] Hendrickson, W.A. Atomic-level analysis of membrane-protein structure. Nat. Struct. Mol. Biol. 2016, 23, 464–467.

[16] Zhou, H.-X., & Cross, T.A. Modeling the membrane environment has implications for membrane protein structure and function: influenza A M2 protein. Protein Sci. 2013, 22, 381–394.

[17] Ujwal, R., & Bowie, J.U. Crystallizing membrane proteins using lipidic bicelles. Methods. 2011, 55, 337–341.

[18] Ishchenko, A., Abola, E.E., & Cherezov, V. Crystallization of membrane proteins: an overview. Methods Mol. Biol. 2017, 1607, 117–141.

[19] Pebay-Peyroula, E., Rummel, G., Rosenbusch, J.P., & Landau, E.M. X-ray structure of bacteriorhodopsin at 2.5 angstroms from microcrystals grown in lipidic cubic phases. Science. 1997, 277, 1676–1681.

[20] Caffrey, M. A comprehensive review of the lipid cubic phase or in meso method for crystallizing membrane and soluble proteins and complexes. Acta. Crystallogr. F. Struct. Biol. Commun. 2015, 71, 3–18.

[21] Cherezov, V. Lipidic cubic phase technologies for membrane protein structural studies. Curr. Opin. Struct. Biol. 2011, 21, 559–566.

[22] Wadsten, P., Wöhri, A.B., Snijder, A., et al. Lipidic sponge phase crystallization of membrane proteins. J. Mol. Biol. 2006, 364, 44–53.

[23] Jiang, Y., & Kalodimos, C.G. NMR studies of large proteins. J. Mol. Biol. 2017, 429, 2667–2676.

[24] Liang, B., & Tamm, L.K. NMR as a tool to investigate the structure, dynamics and function of membrane proteins. Nat. Struct. Mol. Biol. 2016, 23, 468–474.

[25] Wylie, B.J., Do, H.Q., Borcik, C.G., & Hardy, E.P. Advances in solid-state NMR of membrane proteins. Mol. Phys. 2016, 114, 3598–3609.

[26] Opella, S.J., & Marassi, F.M. Structure determination of membrane proteins by NMR spectroscopy. Chem. Rev. 2004, 104, 3587–3606.

[27] Radoicic, J., Lu, G.J., & Opella, S.J. NMR structures of membrane proteins in phospholipid bilayers. Quart. Rev. Biophys. 2014, 47, 249–283.

[28] Nogales, E. The development of cryo-EM into a mainstream structural biology technique. Nat. Methods. 2016, 13, 24–27.

[29] Brun, A., Darwish, T.A., & James, M. Studies of biomimetic cellular membranes using neutron reflection. J. Chem. Biol. Interfaces. 2013, 1, 3–24.

[30] Majkrzak, C.F., Berk, N.F., Krueger, S., & Perez-Salas, U. Structural Investigations of Membranes in Biology by Neutron Reflectometry, in: F.J.T. Gutberlet, & J. Katsaras. (Eds.), Neutron Scattering in Biology, Springer, Berlin, Heidelberg, 2008, pp. 225–263.

[31] Lakey, J.H. Neutrons for biologists: a beginner's guide, or why you should consider using neutrons. J. R. Soc. Interface. 2009, 6, S567–S573.

[32] Fragneto, G., & Gabel, F. Editorial on the topical issue "neutron biological physics". Eur. Phys. J. E, Soft Matter. 2013, 36, 81.
[33] Heinrich, F., & Lösche, M. Zooming in on disordered systems: neutron reflection studies of proteins associated with fluid membranes. Biochim. Biophys. Acta. 2014, 1838, 2341–2349.
[34] Nanda, H., Resolving Membrane-Bound Protein Orientation and Conformation by Neutron Reflectivity, in: J. M. Ruso, & Piñeiro. Á. (Eds.), Proteins in Solution and at Interfaces. Methods and Application in Biotechnology and Materials Science., Wiley, 2013, pp. 99–111.
[35] Junghans, A., Watkins, E.B., Barker, R.D., et al. Analysis of biosurfaces by neutron reflectometry: from simple to complex interfaces. Biointerphases. 2015, 10, 019014.
[36] Teixeira, S.C.M., Ankner, J., Bellissent-Funel, M.C., et al. New sources and instrumentation for neutrons in biology. Chem. Phys. 2008, 345, 133–151.
[37] Dura, J.A., Pierce, D.J., Majkrzak, C.F., et al. AND/R: advanced neutron diffractometer/ reflectometer for investigation of thin films and multilayers for the life sciences. Rev. Sci. Instrum. 2006, 77, 74301–7430111.
[38] Kirby, B.J., Kienzle, P.A., Maranville, B.B., et al. Phase-sensitive specular neutron reflectometry for imaging the nanometer scale composition depth profile of thin-film materials. Curr. Opin. Colloid & Interface Sci. 2012, 17, 44–53.
[39] Pfefferkorn, C.M., Heinrich, F., Sodt, A.J., Maltsev, A.S., Pastor, R.W., & Lee, J.C. Depth of α-synuclein in a bilayer determined by fluorescence, neutron reflectometry, and computation. Biophys. J. 2012, 102, 613–621.
[40] Jiang, Z., Heinrich, F., McGlinchey, R.P., Gruschus, J.M., & Lee, J.C. Segmental deuteration of α-Synuclein for neutron reflectometry on tethered bilayers. J. Phys. Chem. Lett. 2017, 8, 29–34.
[41] Zimmermann, K., Eells, R., Heinrich, F., et al. The cytosolic domain of T-cell receptor ζ associates with membranes in a dynamic equilibrium and deeply penetrates the bilayer. J. Biol. Chem. 2017, 292, 17746–17759.
[42] Hellstrand, E., Grey, M., Ainalem, M.-L., et al. Adsorption of α-Synuclein to supported lipid bilayers: positioning and role of electrostatics. ACS. Chem. Neurosci. 2013, 4, 1339–1351.
[43] Jones, E.M., Dubey, M., Camp, P.J., et al. Interaction of tau protein with model lipid membranes induces tau structural compaction and membrane disruption. Biochemistry. 2012, 51, 2539–2550.
[44] Junghans, A., Watkins, E.B., Majewski, J., Miranker, A., & Stroe, I. Influence of the human and rat islet amyloid polypeptides on structure of phospholipid bilayers: neutron reflectometry and fluorescence microscopy studies. Langmuir. 2016, 32, 4382–4391.
[45] Shenoy, S., Shekhar, P., Heinrich, F., et al. Membrane association of the PTEN tumor suppressor: molecular details of the protein-membrane complex from SPR binding studies and neutron reflection. PLoS ONE. 2012, 7, e32591.
[46] Eells, R., Barros, M., Scott, K.M., Karageorgos, I., Heinrich, F., & Lösche, M., Structural characterization of membrane-bound human immunodeficiency virus-1 Gag matrix with neutron reflectometry. Biointerphases. 2017, 12, 02D408.
[47] Kent, M.S., Murton, J.K., Sasaki, D.Y., et al. Neutron reflectometry study of the conformation of HIV Nef bound to lipid membranes. Biophys. J. 2010, 99, 1940–1948.
[48] Fritz, K., Fritz, G., Windschiegl, B., Steinem, C., & Nickel, B. Arrangement of Annexin A2 tetramer and its impact on the structure and diffusivity of supported lipid bilayers. Soft Matter. 2010, 6, 4084–4094.
[49] Heinrich, F., Nanda, H., Goh, H.Z., Bachert, C., Lösche, M., & Linstedt, A.D. Myristoylation restricts orientation of the GRASP domain on membranes and promotes membrane tethering. J. Biol. Chem. 2014, 289, 9683–9691.

[50] Brouette, N., Fragneto, G., Cousin, F., Moulin, M., Haertlein, M., & Sferrazza, M. A neutron reflection study of adsorbed deuterated myoglobin layers on hydrophobic surfaces. J. Colloid Interface Sci. 2013, 390, 114–120.
[51] Nanda, H., Datta, S.A.K., Heinrich, F., et al. Electrostatic interactions and binding orientation of HIV-1 matrix studied by neutron reflectivity. Biophys. J. 2010, 99, 2516–2524.
[52] Datta, S.A.K., Heinrich, F., Raghunandan, S., et al. HIV-1 Gag extension: conformational changes require simultaneous interaction with membrane and nucleic acid. J. Mol. Biol. 2011, 406, 205–214.
[53] Le Brun, A.P., Holt, S.A., Shah, D.S., Majkrzak, C.F., & Lakey, J.H. Monitoring the assembly of antibody-binding membrane protein arrays using polarised neutron reflection. Eur. Biophys. J. 2008, 37, 639–645.
[54] Kreiner, M., Chillakuri, C.R., Pereira, P., et al. Orientation and surface coverage of adsorbed fibronectin cell binding domains and bound integrin alpha α5β1 receptors. Soft Matter. 2009, 5, 3954–3962.
[55] Le Brun, A.P., Holt, S.A., Shah, D.S.H., Majkrzak, C.F., & Lakey, J.H. The structural orientation of antibody layers bound to engineered biosensor surfaces. Biomaterials. 2011, 32, 3303–3311.
[56] Hoogerheide, D.P., Noskov, S.Y., Jacobs, D., et al. Structural features and lipid binding domain of tubulin on biomimetic mitochondrial membranes. Proc. Natl. Acad. Sci. U.S.A. 2017, 114, E3622–E3631.
[57] Hossain, K.R., Holt, S.A., Le Brun, A.P., Khamici Al, H., Valenzuela, S.M. X-ray and neutron reflectivity study shows that CLIC1 undergoes cholesterol-dependent structural reorganization in lipid monolayers. Langmuir. 2017, 33, 12497–12509.
[58] Yap, T.L., Jiang, Z., Heinrich, F., et al. Structural features of membrane-bound glucocerebrosidase and α-synuclein probed by neutron reflectometry and fluorescence spectroscopy. J. Biol. Chem. 2015, 290, 744–754.
[59] McGillivray, D.J., Valincius, G., Vanderah, D.J., et al. Molecular-scale structural and functional characterization of sparsely tethered bilayer lipid membranes. Biointerphases. 2007, 2, 21–33.
[60] Heinrich, F., Ng, T., Vanderah, D.J., et al. A new lipid anchor for sparsely tethered bilayer lipid membranes. Langmuir. 2009, 25, 4219–4229.
[61] Budvytyte, R., Valincius, G., Niaura, G., et al. Structure and properties of tethered bilayer lipid membranes with unsaturated anchor molecules. Langmuir. 2013, 29, 8645–8656.
[62] Vockenroth, I.K., Ohm, C., Robertson, J.W.F., McGillivray, D.J., Lösche, M., & Köper, I. Stable insulating tethered bilayer lipid membranes. Biointerphases. 3, 2008, FA68.
[63] Fragneto, G. Neutrons and model membranes. Eur. Phys. J-Spec. Top. 2012, 213, 327–342.
[64] Shekhar, P., Nanda, H., Lösche, M., & Heinrich, F. Continuous distribution model for the investigation of complex molecular architectures near interfaces with scattering techniques. J. Appl. Phys. 2011, 110, 102216-1–102216-12.
[65] Belicka, M., Gerelli, Y., Kučerka, N., & Fragneto, G. The component group structure of DPPC bilayers obtained by specular neutron reflectometry. Soft Matter. 2015, 11, 6275–6283.
[66] McGillivray, D.J., Valincius, G., Heinrich, F., et al. Structure of functional Staphylococcus aureus α-hemolysin channels in tethered bilayer lipid membranes. Biophys. J. 2009, 96, 1547–1553.
[67] Shenoy, S.S., Nanda, H., & Lösche, M. Membrane association of the PTEN tumor suppressor: electrostatic interaction with phosphatidylserine-containing bilayers and regulatory role of the C-terminal tail. J. Struct. Biol. 2012, 180, 394–408.
[68] Smith, G.S., & Majkrzak, C.F. Neutron reflectometry, in: E. Prince, H. Fuess, T. Hahn, et al. (Eds.), International Tables for Crystallography, 1st ed., International Union of Crystallography, Chester, England 2006, pp. 126–146.

[69] Ankner, J.F., & Majkrzak, C.F. Subsurface profile refinement for neutron specular reflectivity. SPIE. Proc. 1992, 1738, 260–269.
[70] Penfold, J., Richardson, R.M., Zarbakhsh, A., et al. Recent advances in the study of chemical surfaces and interfaces by specular neutron reflection. J. Chem. Soc. Faraday Trans. 1997, 93, 3899–3917.
[71] Russell, T.P. X-ray and neutron reflectivity for the investigation of polymers. Mater. Sci. Rep. 1990, 5, 171–271.
[72] Fragneto, G., Thomas, R.K., Rennie, A.R., & Penfold, J. Neutron reflection study of bovine β-casein adsorbed on OTS self-assembled monolayers. Science. 1995, 267, 657–660.
[73] Wacklin, H.P. Neutron reflection from supported lipid membranes. Curr. Opin. Colloid & Interface Sc. 2010, 15, 445–454.
[74] Daillant, J. Recent developments and applications of grazing incidence scattering. Curr. Opin. Colloid & Interface Sci. 2009, 14, 396–401.
[75] Kučerka, N., Nieh, M.-P., Pencer, J., Harroun, T., & Katsaras, J. The study of liposomes, lamellae and membranes using neutrons and X-rays. Curr. Opin. Colloid & Interface Sci. 2007, 12, 17–22.
[76] Lovell, M.R., & Richardson, R.M. Analysis methods in neutron and X-ray reflectometry. Curr. Opin. Colloid & Interface Sci. 1999, 4, 197–204.
[77] Lu, J.R., Zhao, X., & Yaseen, M. Protein adsorption studied by neutron reflection. Curr. Opin. Colloid & Interface Sci. 2007, 12, 9–16.
[78] Schlossman, M.L. Liquid-liquid interfaces: studied by X-ray and neutron scattering. Curr. Opin. Colloid & Interface Sci. 2002, 7, 235–243.
[79] Thomas, R.K., & Penfold, J. Neutron and X-ray reflectometry of interfacial systems in colloid and polymer chemistry. Curr. Opin. Colloid & Interface Sci. 1996, 1, 23–33.
[80] Als-Nielsen, J., & Kjær, K. X-Ray Reflectivity and Diffraction Studies of Liquid Surfaces and Surfactant Monolayers, in: Phase Transitions in Soft Condensed Matter, Springer, Boston, MA, New York 1989, pp. 113–138.
[81] Majkrzak, C.F., Metting, C., Maranville, B.B., et al. Determination of the effective transverse coherence of the neutron wave packet as employed in reflectivity investigations of condensed-matter structures. I. Measurements. Phys. Rev. A. 2014, 89, 033851.
[82] Cohen-Tannoudji, C., Diu, B., & Laloe, F. Quantum Mechanics, Wiley-VCH, New York 1992.
[83] Sears, V.F. Neutron scattering lengths and cross sections. Neutron News. 1992, 3, 26–37.
[84] Majkrzak, C.F., Berk, N.F., & Perez-Salas, U. Phase-sensitive neutron reflectometry. Langmuir. 2003, 19, 7796–7810.
[85] Song, L., Hobaugh, M.R., Shustak, C., Cheley, S., Bayley, H., & Gouaux, J.E. Structure of staphylococcal α-hemolysin, a heptameric transmembrane pore. Science. 1996, 274, 1859–1866.
[86] Majkrzak, C.F., Carpenter, E., Heinrich, F., & Berk, N.F. When beauty is only skin deep; optimizing the sensitivity of specular neutron reflectivity for probing structure beneath the surface of thin films. J. Appl. Phys. 2011, 110, 102212.
[87] Majkrzak, C.F., & Berk, N.F. Exact determination of the phase in neutron reflectometry. Phys. Rev. B. 1995, 52, 10827–10830.
[88] Dehaan, V.O., van Well, A.A., Adenwalla, S., & Felcher, G.P. Retrieval of phase information in neutron reflectometry. Phys. Rev. B. 1995, 52, 10831–10833.
[89] Majkrzak, C.F., & Berk, N.F. Exact determination of the phase in neutron reflectometry by variation of the surrounding media. Phys. Rev. B. 1998, 58, 15416–15418.
[90] Majkrzak, C.F., Berk, N.F., Krueger, S., et al. First-principles determination of hybrid bilayer membrane structure by phase-sensitive neutron reflectometry. Biophys. J. 2000, 79, 3330–3340.

[91] Majkrzak, C.F., & Berk, N.F. Phase sensitive reflectometry and the unambiguous determination of scattering length density profiles. Physica. B. 2003, 336, 27–38.
[92] Majkrzak, C.F., Berk, N.F., Kienzle, P., & Perez-Salas, U. Progress in the development of phase-sensitive neutron reflectometry methods. Langmuir. 2009, 25, 4154–4161.
[93] Valincius, G., Heinrich, F., Budvytyte, R., et al. Soluble amyloid β-oligomers affect dielectric membrane properties by bilayer insertion and domain formation: implications for cell toxicity. Biophys. J. 2008, 95, 4845–4861.
[94] Valincius, G., Meškauskas, T., & Ivanauskas, F. Electrochemical impedance spectroscopy of tethered bilayer membranes. Langmuir. 2012, 28, 977–990.
[95] Barros, M., Heinrich, F., Datta, S.A.K., et al. Membrane binding of HIV-1 matrix protein: dependence on bilayer composition and protein lipidation. J. Virol. 2016, 90, 4544–4555.
[96] Chan, Y.-H.M., & Boxer, S.G. Model membrane systems and their applications. Curr. Opin. Chem. Biol. 2007, 11, 581–587.
[97] Khan, M.S., Dosoky, N.S., & Williams, J.D. Engineering lipid bilayer membranes for protein studies. Int. J. Mol. Sci. 2013, 14, 21561–21597.
[98] Weygand, M., Wetzer, B., Pum, D., et al. Bacterial S-layer protein coupling to lipids: x-ray reflectivity and grazing incidence diffraction studies. Biophys. J. 1999, 76, 458–468.
[99] Tietjen, G.T., Gong, Z., Chen, C.-H., et al. Molecular mechanism for differential recognition of membrane phosphatidylserine by the immune regulatory receptor Tim4. Proc. Natl. Acad. Sci. USA. 2014, 111, E1463–14672.
[100] Tietjen, G.T., Baylon, J.L., Kerr, D., et al. Coupling X-Ray reflectivity and in silico binding to yield dynamics of membrane recognition by Tim1. Biophys. J. 2017, 113, 1505–1519.
[101] Vaknin, D., Als-Nielsen, J., Piepenstock, M., & Lösche, M. Recognition processes at a functionalized lipid surface observed with molecular resolution. Biophys. J. 1991, 60, 1545–1552.
[102] Lösche, M., Piepenstock, M.M., Diederich, A.A., Grünewald, T.T., Kjær, K., & Vaknin, D. Influence of surface chemistry on the structural organization of monomolecular protein layers adsorbed to functionalized aqueous interfaces. Biophys. J. 1993, 65, 2160–2177.
[103] Akgun, B., Satija, S., Nanda, H., et al. Conformational transition of membrane-associated terminally acylated HIV-1 nef. Structure. 2013, 21, 1822–1833.
[104] Schalke, M., & Lösche, M. Structural models of lipid surface monolayers from X-ray and neutron reflectivity measurements. Adv. Colloid Interface. 2000, 88, 243–274.
[105] Wiener, M.C., & White, S.H. Structure of a fluid dioleoylphosphatidylcholine bilayer determined by joint refinement of x-ray and neutron diffraction data. III. Complete structure. Biophys. J. 1992, 61, 434–447.
[106] Nagle, J.F., & Tristram-Nagle, S. Structure of lipid bilayers. Biochim. Biophys. Acta. 2000, 1469, 159–195.
[107] Liu, Y., & Nagle, J.F. Diffuse scattering provides material parameters and electron density profiles of biomembranes. Phys. Rev. E. 2004, 69, 40901.
[108] Cruz, J., Mihailescu, M., Wiedman, G., et al. A membrane-translocating peptide penetrates into bilayers without significant bilayer perturbations. Biophys. J. 2013, 104, 2419–2428.
[109] Tristram-Nagle, S.A., Chan, R., Kooijman, E., et al. HIV fusion peptide penetrates, disorders, and softens T-cell membrane mimics. J. Mol. Biol. 2010, 402, 139–153.
[110] Hardy, G.J., Nayak, R., Munir Alam, S., Shapter, J.G., Heinrich, F., & Zauscher, S. Biomimetic supported lipid bilayers with high cholesterol content. J. Mater. Chem. 2012, 22, 19506–19513.
[111] Benedetto, A., Heinrich, F., Gonzalez, M.A., Fragneto, G., Watkins, E., & Ballone, P. Structure and stability of phospholipid bilayers hydrated by a room-temperature ionic liquid/water solution: a neutron reflectometry study. J. Phys. Chem. B. 2014, 118, 12192–12206.

[112] Meuse, C.W., Krueger, S., Majkrzak, C.F., et al. Hybrid bilayer membranes in air and water: infrared spectroscopy and neutron reflectivity studies. Biophys. J. 1998, 74, 1388–1398.
[113] Krueger, S., Meuse, C.W., Majkrzak, C.F., et al. Investigation of hybrid bilayer membranes with neutron reflectometry: probing the interactions of melittin. Langmuir. 2001, 17, 511–521.
[114] Anderson, N.A., Richter, L.J., Stephenson, J.C., & Briggman, K.A. Determination of lipid phase transition temperatures in hybrid bilayer membranes. Langmuir. 2006, 22, 8333–8336.
[115] Anderson, N.A., Richter, L.J., Stephenson, J.C., & Briggman, K.A. Characterization and control of lipid layer fluidity in hybrid bilayer membranes. J. Am. Chem. Soc. 2007, 129, 2094–2100.
[116] Köper, I. Insulating tethered bilayer lipid membranes to study membrane proteins. Mol. Biosyst. 2007, 3, 651–657.
[117] Junghans, A., & Köper, I. Structural analysis of tethered bilayer lipid membranes. Langmuir. 2010, 26, 11035–11040.
[118] Rossi, C., & Chopineau, J. Biomimetic tethered lipid membranes designed for membrane-protein interaction studies. Eur. Biophys. J. 2007, 36, 955–965.
[119] Andersson, J., Knobloch, J.J., Perkins, M.V., Holt, S.A., & Köper, I. Synthesis and characterization of novel anchorlipids for tethered bilayer lipid membranes. Langmuir. 2017, 33, 4444–4451.
[120] Wagner, M.L., & Tamm, L.K. Tethered polymer-supported planar lipid bilayers for reconstitution of integral membrane proteins: silane-polyethyleneglycol-lipid as a cushion and covalent linker. Biophys. J. 2000, 79, 1400–1414.
[121] Naumann, C.A., Prucker, O., Lehmann, T., Ruhe, J., Knoll, W., & Frank, C.W. The polymer-supported phospholipid bilayer: tethering as a new approach to substrate-membrane stabilization. Biomacromolecules. 2002, 3, 27–35.
[122] Tanaka, M., & Sackmann, E. Polymer-supported membranes as models of the cell surface. Nature. 2005, 437, 656–663.
[123] Jablin, M.S., Zhernenkov, M. Toperverg, B.P., et al. In-plane correlations in a polymer-supported lipid membrane measured by off-specular neutron scattering. Phys. Rev. Lett. 2011, 106, 138101.
[124] Singh, S., Junghans, A., Tian, J., et al. Polyelectrolyte multilayers as a platform for pH-responsive lipid bilayers. Soft Matter. 2013, 9, 8938–8948.
[125] Fragneto, G., Charitat, T., Graner, F., Mecke, K., Perino-Gallice, L., & Bellet-Amalric, E. A fluid floating bilayer. Epl-Europhys. Lett. 2001, 53, 100–106.
[126] Hughes, A.V., Howse, J.R., Dabkowska, A., Jones, R., Lawrence, M.J., & Roser, S.J. Floating lipid bilayers deposited on chemically grafted phosphatidylcholine surfaces. Langmuir. 2008, 24, 1989–1999.
[127] Schiller, S.M., Naumann, R., Lovejoy, K., Kunz, H., & Knoll, W. Archaea analogue thiolipids for tethered bilayer lipid membranes on ultrasmooth gold surfaces. Angew. Chem. Int. Ed. Engl. 2003, 42, 208–211.
[128] Vockenroth, I.K., Atanasova, P.P., Jenkins, A.T.A., & Köper, I. Incorporation of alpha-hemolysin in different tethered bilayer lipid membrane architectures. Langmuir. 2008, 24, 496–502.
[129] Vockenroth, I.K., Rossi, C., Shah, M.R., & Köper, I. Formation of tethered bilayer lipid membranes probed by various surface sensitive techniques. Biointerphases. 2009, 4, 19–26.
[130] Shenoy, S., Moldovan, R., Fitzpatrick, J., Vanderah, D.J., Deserno, M., & Lösche, M. In-plane homogeneity and lipid dynamics in tethered bilayer lipid membranes (tBLMs). Soft Matter. 2010, 2010, 1263–1274.
[131] van Meer, G., Voelker, D.R., & Feigenson, G.W. Membrane lipids: where they are and how they behave. Nat. Rev. Mol. Cell. Biol. 2008, 9, 112–124.

[132] Lomize, M.A., Pogozheva, I.D., Joo, H., Mosberg, H.I., & Lomize, A.L. OPM database and PPM web server: resources for positioning of proteins in membranes. Nucleic Acids Res. 2012, 40, D370–D376.
[133] Whited, A.M., & Johs, A. The interactions of peripheral membrane proteins with biological membranes. Chem. Phys. Lipids. 2015, 192, 51–59.
[134] Cornell, B.A., Braach-Maksvytis, V., King, L.G., et al. A biosensor that uses ion-channel switches. Nature. 1997, 387, 580–583.
[135] Hardy, G.J., Nayak, R., & Zauscher, S. Model cell membranes: techniques to form complex biomimetic supported lipid bilayers via vesicle fusion. Curr. Opin. Colloid & Interface Science. 2013, 18, 448–458.
[136] Seitz, M., Ter-Ovanesyan, E., Hausch, M., et al. Formation of tethered supported bilayers by vesicle fusion onto lipopolymer monolayers promoted by osmotic stress. Langmuir. 2000, 16, 6067–6070.
[137] Kwak, K.J., Valincius, G., Liao, W.-C., et al. Formation and finite element analysis of tethered bilayer lipid structures. Langmuir. 2010, 26, 18199–18208.
[138] Barsoukov, E., & Macdonald, J.R. (Eds.). Impedance Spectroscopy, John Wiley & Sons, Inc, New Jersey 2005.
[139] Valincius, G., Mickevicius, M., Penkauskas, T., & Jankunec, M. Electrochemical impedance spectroscopy of tethered bilayer membranes: an effect of heterogeneous distribution of defects in membranes. Electrochim. Acta. 2016, 222, 904–913.
[140] Cho, W.W., Bittova, L., & Stahelin, R.V. Membrane binding assays for peripheral proteins. Anal. Biochem. 2001, 296, 153–161.
[141] Richter, R.P., Him, J.L.K., Tessier, B., Tessier, C., & Brisson, A.R. On the kinetics of adsorption and two-dimensional self-assembly of annexin A5 on supported lipid bilayers. Biophys. J. 2005, 89, 3372–3385.
[142] Rodahl, M., Höök, F., Fredriksson, C., et al. Simultaneous frequency and dissipation factor QCM measurements of biomolecular adsorption and cell adhesion. Faraday Discuss. 1997, 107, 229–246.
[143] Knoll, W. Interfaces and thin films as seen by bound electromagnetic waves. Annu. Rev. Phys. Chem. 1998, 49, 569–638.
[144] Löfås, S., Malmqvist, M., Rönnberg, I., Stenberg, E., Liedberg, B., & Lundström, I. Bioanalysis with surface plasmon resonance. Sens. Actuators B: Chem. 1991, 5, 79–84.
[145] Pattnaik, P. Surface plasmon resonance - Applications in understanding receptor-ligand interaction. Appl. Biochem. Biotechnol. 2005, 126, 79–92.
[146] Wei, Y., & Latour, R.A. Determination of the adsorption free energy for peptide-surface interactions by SPR spectroscopy. Langmuir. 2008, 24, 6721–6729.
[147] Hinderliter, A., & May, S. Cooperative adsorption of proteins onto lipid membranes. J. Phys.: Condens. Matter 2006, 18, S1257–S1270.
[148] Minton, A.P. Effects of excluded surface area and adsorbate clustering on surface adsorption of proteins. II. Kinetic models. Biophys. J. 2001, 80, 1641–1648.
[149] May, S., Harries, D., & Ben-Shaul, A. Lipid demixing and protein-protein interactions in the adsorption of charged proteins on mixed membranes. Biophys. J. 2000, 79, 1747–1760.
[150] Heimburg, T., Angerstein, B., & Marsh, D. Binding of peripheral proteins to mixed lipid membranes: effect of lipid demixing upon binding. Biophys. J. 1999, 76, 2575–2586.
[151] Weiss, J.N. The Hill equation revisited: uses and misuses. Faseb J. 1997, 11, 835–841.
[152] Murray, D., Ben-Tal, N., Honig, B., & McLaughlin, S. Electrostatic interaction of myristoylated proteins with membranes: simple physics, complicated biology. Struct./Folding Des. 1997, 5, 985–989.

[153] Ben-Shaul, A., Ben-Tal, N., & Honig, B. Statistical thermodynamic analysis of peptide and protein insertion into lipid membranes. Biophys. J. 1996, 71, 130–137.
[154] Heinrich, F. Deuteration in biological neutron reflectometry. Methods in Enzymol. 2016, 566, 211–230.
[155] Sivia, D.S., & Webster, J. The Bayesian approach to reflectivity data. Physica B. 1998, 248, 327–337.
[156] Jiang, Z., Hess, S.K., Heinrich, F., & Lee, J.C. Molecular details of alpha-synuclein membrane association revealed by neutrons and photons. J. Phys. Chem. B. 2015, 119, 4812–4823.
[157] Majkrzak, C.F., O'Donovan, K.V., & Berk, N.F. (2006). Polarized Neutron Reflectometry. In T. Chatterji (Ed.), *Neutron Scattering from Magnetic Materials* (pp. 397–471). Amsterdam, Boston, Heidelberg, London, New York, Oxford, Paris, San Diego, San francisco, Singapore, Syney, Tokyo: Elsevier. http://doi.org/10.1016/B978-044451050-1/50010-0
[158] Maranville, B.B. Interactive, web-based calculator of neutron and X-ray reflectivity. J. Res. Natl. Inst. Stand. Technol. 2017, 122, 34.
[159] Maranville, B.B., Kirby, B.J., Grutter, A.J., et al. Measurement and modeling of polarized specular neutron reflectivity in large magnetic fields. J. Appl. Crystallogr. 2016, 49, 1121–1129.
[160] de Haan, V., & Drijkoningen, G. Genetic algorithms used in model finding and fitting for neutron reflection experiments. Physica B. 1994, 198, 24–26.
[161] Braak, T. Cajo, J.F. A Markov Chain Monte Carlo version of the genetic algorithm differential evolution: easy Bayesian computing for real parameter spaces. Stat. Comput. 2006, 16, 239–249.
[162] Braak, T., Vrugt, J.A., & Cajo, J.F. Differential Evolution Markov Chain with snooker updater and fewer chains. Stat. Comput. 2008, 18, 435–446.
[163] Samoilenko, I., Feigin, L., Shchedrin, B., & Antolini, R. Selection of a model in reflectometry: use of the linear statistical inference. Physica B. 2000, 283, 262–267.
[164] Nelson, A. Co-refinement of multiple-contrast neutron/X-ray reflectivity data using MOTOFIT. J. Appl. Crystallogr. 2006, 39, 273–276.
[165] van der Lee, A., Salah, F., & Harzallah, B. A comparison of modern data analysis methods for X-ray and neutron specular reflectivity data. J. Appl. Crystallogr. 2007, 40, 820–833.
[166] Gerelli, Y. Aurore: new software for neutron reflectivity data analysis. J. Appl. Crystallogr. 2016, 49, 330–339.
[167] Wiener, M.C., & White, S.H. Fluid bilayer structure determination by the combined use of x-ray and neutron diffraction. II. "Composition-space" refinement method. Biophys. J. 1991, 59, 174–185.
[168] Connolly, M.L. Solvent-accessible surfaces of proteins and nucleic acids. Science. 1983, 221, 709–713.
[169] Connolly, M.L. Analytical molecular surface calculation. J. Appl. Crystallogr. 1983, 16, 548–558.
[170] Perkins, S.J. Protein volumes and hydration effects. The calculations of partial specific volumes, neutron scattering matchpoints and 280 nm absorption coefficients for proteins and glycoproteins from amino acid sequences. Eur. J. Biochem. 1986, 157, 169–180.
[171] Curtis, J.E., Zhang, H., & Nanda, H. SLDMOL: a tool for the structural characterization of thermally disordered membrane proteins. Comput. Phys. Commun. 2014, 185, 3010–3015.
[172] Hughes, A.V., Ciesielski, F., Kalli, A.C., et al. On the interpretation of reflectivity data from lipid bilayers in terms of molecular-dynamics models. Acta. Crystallogr. D. Struct. Biol. 2016, 72, 1227–1240.
[173] Nettles, J.H., Li, H.L., Cornett, B., Krahn, J.M., Snyder, J.P., & Downing, K.H. The binding mode of epothilone A on α,β-tubulin by electron crystallography. Science. 2004, 305, 866–869.